J. Fluid Mech. (2010), *vol.* 652, *pp.* 461–488.
doi:10.1017/S0022112010000315

Rapid granular flows down inclined planar chutes. Part 2. Linear stability analysis of steady flow solutions

MARK J. WOODHOUSE† AND ANDREW J. HOGG

Department of Mathematics, University of Bristol, University Walk, Bristol BS8 1TW, UK

(Received 28 May 2009; revised 14 January 2010; accepted 15 January 2010)

The linear stability of steady solutions for a rapid granular flow down an inclined chute, modelled using a kinetic theory continuum model, is analysed. The previous studies of Forterre & Pouliquen (*J. Fluid Mech.*, vol. 467, 2002, p. 361) and Mitarai & Nakanishi (*J. Fluid Mech.*, vol. 507, 2004, p. 309) are extended by considering fully three-dimensional perturbations, allowing variations in both the cross-slope and downslope directions, as well as normal to the base. Our results demonstrate the existence of three qualitatively different unstable perturbations, each of which can be the most rapidly growing instability for different steady flows. By considering the linear stability of many steady solutions along macroscopic flow curves, we show that linear stability occurs in only a small part of parameter space, and furthermore the regions of linear instability do not correlate with density inversion of the underlying steady solutions. Our results suggest that inelastic clustering is the dominant instability mechanism.

1. Introduction

In this paper, we further analyse rapid granular flows down inclined planar chutes, extending the results reported in Woodhouse, Hogg & Sellar (2010, subsequently referred to as Part 1). Our model adopts kinetic theory, adapted to describe inelastic collisions between particles, to provide a continuum description of the highly agitated flow. In Part 1, we determined solutions corresponding to a steady, fully developed flow down the chute and investigated the character of these solutions as the controlling parameters are varied. Here we assess the linear stability of these solutions to small perturbations, focusing in particular on those parameter values that give rise to multiple flow solutions for a given mass flux of material. An aim of this study is to determine which of the steady solutions we calculate, if any, are linearly stable and thus could be realized in experiments or simulations.

The experiments of Forterre & Pouliquen (2001) demonstrate the potential for pattern forming instabilities to occur in rapid granular chute flows, with longitudinal streaks occurring on the surface of the flowing layer. These streaks are interpreted as the surface deformation caused by the formation of longitudinal vortices in the interior of the flow. Furthermore, Forterre & Pouliquen (2002) show that a more complex pattern of rectangular 'scales' can also occur, which may represent a development

† Present address: School of Mathematics, Alan Turing Building, University of Manchester, Oxford Road, Manchester M13 9PL, UK.
Email address for correspondence: mark.woodhouse@manchester.ac.uk

of the streaks or a separate unstable mode. Instabilities of granular flows have also been seen in discrete element simulations, in both unbounded domains (see e.g. Hopkins & Louge 1991; Goldhirsch & Zanetti 1993; McNamara & Young 1994; Tan & Goldhirsch 1997) and for shear flows in bounded geometries (e.g. Liss, Conway & Glasser 2002; Conway & Glasser 2004). For a gravity-driven flow on an inclined chute (the geometry considered here) a discrete element simulation has been performed by Mitarai & Nakanishi (2001) on a large computational domain, and they uncovered the signature of a clustering instability, with streamwise variations in density appearing along the chute.

Theoretical investigations of the linear stability of rapid granular flows have concentrated on shear flows in unbounded domains (see Savage 1992; Schmid & Kytömaa 1994) and confined geometries (see e.g. Wang, Jackson & Sundaresan 1996, 1997; Alam & Nott 1998; Alam *et al.* 2005; Alam 2006). For an inclined chute geometry, Forterre & Pouliquen (2002) performed a linear stability analysis of a kinetic theory continuum model in order to rationalize their earlier experimental observations. As the experimentally observed instability results in a cross-slope structure, the analysis of Forterre & Pouliquen (2002) was limited to cross-slope perturbations. Their analysis revealed the existence of unstable perturbations with a vortical structure. As these instabilities were discovered as unstable perturbations to steady profiles exhibiting a density inversion, where the steady flow density profile has a maximum occurring in the interior of the flow, and where the base of the flow is a source of fluctuation energy, Forterre & Pouliquen (2002) proposed a mechanism akin to the well-known Rayleigh–Bénard convection in which a fluid layer heated from below becomes unstable and forms vortices (Drazin & Reid 1981). Mitarai & Nakanishi (2004) followed Forterre & Pouliquen (2002) in their linear stability analysis, but considered perturbations only in the downslope direction in an attempt to reproduce the instability observed in the discrete element simulations of Mitarai & Nakanishi (2001). Again, linearly unstable perturbations were obtained and interpreted by Mitarai & Nakanishi (2004) as density waves that form because of clustering of the inelastic grains.

The analyses of Forterre & Pouliquen (2002) and Mitarai & Nakanishi (2004) show that steady chute flows can be unstable to both purely cross-slope and purely downslope perturbations, respectively. However, it is not clear in advance whether either of these perturbations represents the most rapidly growing instability and so is the dominant mode which may be seen in experiments. Nor is it easy to assess the mechanism by which the instability proceeds. We therefore perform a three-dimensional stability analysis, allowing perturbations to the underlying steady flow with variations in the downslope and cross-slope directions as well as normal to the chute base. Our results establish three qualitatively different linearly unstable perturbations. Two of these occur for purely cross-slope perturbations and of these one is a vortex-forming perturbation similar to that obtained by Forterre & Pouliquen (2002) while the other is a non-vortex-forming clustering instability. The third instability occurs for purely downslope perturbations, similar to that obtained by Mitarai & Nakanishi (2004).

While our methodology is broadly similar to the previous studies of Forterre & Pouliquen (2002) and Mitarai & Nakanishi (2004), there are some important differences. Our analysis shows that the boundary conditions enforced by Forterre & Pouliquen (2002), and subsequently by Mitarai & Nakanishi (2004), at the free surface overprescribe the behaviour of the perturbation fields, and employ additional artificial boundary conditions which are unnecessary. The far-field conditions have

a particularly strong influence at small wavenumbers, for which we often find the most rapidly growing mode. Our analysis also reveals the existence of a continuous spectrum of eigenvalues that can interfere in the numerical calculation of the unstable modes and leads to the requirement of high numerical accuracy in the computation of both the base state and linear stability eigenvalues. We achieve this high accuracy by employing a Chebyshev pseudospectral method, as described in Part 1.

This paper is organized as follows. In § 2 we recall the continuum equations for granular flows and linearize these equations about the steady, fully developed chute flow to obtain evolution equations for small perturbations, which are further simplified by making a normal mode approximation. The algebraic details of these calculations can be found in the Appendix. Typical results are presented in § 3, where we demonstrate the existence of three qualitatively different unstable modes. We also study the linear stability characteristics along macroscopic flow curves, showing that linearly stable solutions exist only on a relatively small segment of the curves and for a limited range of inclination angles. In § 4 we compare our results with the previous studies of Forterre & Pouliquen (2002) and Mitarai & Nakanishi (2004), and discuss the implications of our results for the proposed instability mechanisms. A summary of our investigation is given in § 5.

2. Linearized governing equations

We recall the equations governing the evolution of a rapid granular flow under gravity as

$$\frac{\mathrm{D}\rho}{\mathrm{D}t} = -\rho\nabla\cdot\boldsymbol{u}, \tag{2.1}$$

$$\rho\frac{\mathrm{D}\boldsymbol{u}}{\mathrm{D}t} = \rho\boldsymbol{g} - \nabla\cdot\boldsymbol{P}, \tag{2.2}$$

$$\frac{3}{2}\rho\frac{\mathrm{D}T}{\mathrm{D}t} = -\boldsymbol{P}:\nabla\boldsymbol{u} - \nabla\cdot\boldsymbol{q} - \gamma, \tag{2.3}$$

where $\mathrm{D}/\mathrm{D}t = \partial/\partial t + \boldsymbol{u}\cdot\nabla$ denotes the advective derivative, $\boldsymbol{g}$ is the acceleration due to gravity, $\boldsymbol{P}$ is the pressure tensor, $\boldsymbol{q}$ is the heat flux and γ is the dissipation due to inelastic collisions (Lun *et al.* 1984). These equations represent mass, momentum and fluctuation energy conservation, respectively. The pressure tensor and heat flux are

$$\boldsymbol{P} = (p - \xi(\nabla\cdot\boldsymbol{u}))\boldsymbol{I} - 2\eta\boldsymbol{S}, \tag{2.4}$$

$$\boldsymbol{q} = -K\nabla T + K^*\nabla\nu, \tag{2.5}$$

$$\boldsymbol{S} = \tfrac{1}{2}\left(\nabla\boldsymbol{u} + \nabla\boldsymbol{u}^{\mathrm{T}}\right) - \tfrac{1}{3}(\nabla\cdot\boldsymbol{u})\boldsymbol{I}, \tag{2.6}$$

where $\boldsymbol{I}$ is the identity matrix and $\boldsymbol{S}$ is the deviatoric part of the symmetric strain rate tensor. The pressure p, viscosity η, bulk viscosity ξ, conductivities K and K^*, and dissipation γ are given from a kinetic theory adapted to describe inelastic collisions (here we adopt the constitutive theory of Lun *et al.* 1984) as functions of the volume fraction and granular temperature:

$$\left.\begin{array}{lll} p = g_1(\nu)T, & \eta = g_2(\nu)T^{1/2}, & \xi = g_6(\nu)T^{1/2}, \\ K = g_3(\nu)T^{1/2}, & K^* = g_4(\nu)T^{3/2}, & \gamma = g_5(\nu)T^{3/2}, \end{array}\right\} \tag{2.7}$$

where the dimensionless functions $g_i(\nu)$ are given in Part 1.

In Part 1, we have found solutions of the governing equations corresponding to a steady, fully developed flow. These solutions have been characterized by the

$a_0 = \dot{g}_1(\nu_0)T_0$	$b_0 = g_1(\nu_0)$
$c_0 = \dot{g}_2(\nu_0)T_0^{1/2}$	$d_0 = \frac{1}{2}g_2(\nu_0)T_0^{-1/2}$
$e_0 = \dot{g}_3(\nu_0)T_0^{1/2}$	$h_0 = \frac{1}{2}g_3(\nu_0)T_0^{-1/2}$
$e_0^* = \dot{g}_4(\nu_0)T_0^{3/2}$	$h_0^* = \frac{3}{2}g_4(\nu_0)T_0^{1/2}$
$l_0 = \dot{g}_5(\nu_0)T_0^{3/2}$	$m_0 = \frac{3}{2}g_5(\nu_0)T_0^{1/2}$

TABLE 1. Functions of the steady solutions required for the linear stability analysis. Note that $\dot{g}_i = \mathrm{d}g_i/\mathrm{d}\nu$.

macroscopic (dimensionless) mass flux Q_0, mass hold-up M_0, and centre-of-mass h_0, defined as the depth-integrated quantities:

$$Q_0 = \int_0^\infty \nu_0 u_0 \,\mathrm{d}z, \quad M_0 = \int_0^\infty \nu_0 \,\mathrm{d}z, \quad h_0 = \frac{1}{M_0}\int_0^\infty \nu_0 z \,\mathrm{d}z. \tag{2.8}$$

We have introduced a zero subscript to highlight that these quantities are determined from the steady solutions. Parametric continuation of the steady solutions has shown the existence of multiple steady flow solutions for a fixed mass flux of material in some regions of the parameter space.

We investigate the linear stability of these steady solutions to small perturbations using the classical normal mode analysis (Drazin & Reid 1981). The steady flow solution, denoted by (ν_0, T_0, u_0), is perturbed by a small disturbance such that

$$\left.\begin{aligned} \nu(x,y,z,t) &= \nu_0(z) + \nu_1(x,y,z,t),\\ u(x,y,z,t) &= u_0(z) + u_1(x,y,z,t),\\ v(x,y,z,t) &= v_1(x,y,z,t),\\ w(x,y,z,t) &= w_1(x,y,z,t),\\ T(x,y,z,t) &= T_0(z) + T_1(x,y,z,t). \end{aligned}\right\} \tag{2.9}$$

The pressure, viscosity, conductivities and dissipation are linearized as

$$\left.\begin{aligned} p(\nu,T) &= p_0 + a_0\nu_1 + b_0T_1, \qquad \eta(\nu,T) = \eta_0 + c_0\nu_1 + d_0T_1,\\ K(\nu,T) &= K_0 + e_0\nu_1 + h_0T_1, \quad K^*(\nu,T) = K_0^* + e_0^*\nu_1 + h_0^*T_1,\\ \gamma(\nu,T) &= \gamma_0 + l_0\nu_1 + m_0T_1, \end{aligned}\right\} \tag{2.10}$$

following the notation of Forterre & Pouliquen (2002). Here a zero subscript denotes a quantity that depends only on the steady solution (so $p_0 = p(\nu_0, T_0)$, $\xi_0 = \xi(\nu_0, T_0)$ etc.), and the functions a_0, b_0 etc. are given in table 1. The variables representing the perturbation are denoted by the suffix 1 and are assumed to be much smaller than the steady flow.

The governing equations are linearized (as detailed in the Appendix) about the steady flow and we seek a normal mode solution of the perturbed fields of the form

$$(\nu_1, u_1, v_1, w_1, T_1)(x,y,z,t) = (\hat{\nu}, \hat{u}, \hat{v}, \hat{w}, \hat{T})\mathrm{e}^{\sigma t + \mathrm{i}k_x x + \mathrm{i}k_y y}, \tag{2.11}$$

where the variables $(\hat{\nu}, \hat{u}, \hat{v}, \hat{w}, \hat{T})$ are functions of z. We consider the temporal stability of the steady flow, so specify the disturbance wavenumbers $k_x, k_y \in \mathbb{R}$ and determine the set of growth rates $\sigma \in \mathbb{C}$. On inserting the normal mode ansatz into the linear partial differential equations we obtain a linear system of ordinary differential equations with the growth rate appearing as an eigenvalue, which can be written in

matrix form as

$$\boldsymbol{L}(k_x, k_y)\frac{\mathrm{d}^2\boldsymbol{X}}{\mathrm{d}z^2} + \boldsymbol{M}(k_y, k_y)\frac{\mathrm{d}\boldsymbol{X}}{\mathrm{d}z} + \boldsymbol{N}(k_x, k_x)\boldsymbol{X} = \sigma\boldsymbol{\Sigma}\boldsymbol{X}, \tag{2.12}$$

where $\boldsymbol{X} = (\hat{v}, \hat{u}, \hat{v}, \hat{w}, \hat{T})^{\mathrm{T}}$ and the elements of the matrices $\boldsymbol{L}$, $\boldsymbol{M}$, $\boldsymbol{N}$, $\boldsymbol{\Sigma}$ are functions of the steady solutions and the disturbance wavenumbers, as given in the Appendix. The linearized equations must be augmented with the appropriate linearized boundary conditions at the chute base and the free surface, but first we consider the order of the system of ordinary differential equations.

2.1. *Order of linearized equations and the continuous spectrum*

To determine the order of the linear system of ordinary differential equations, and thus the number of boundary conditions required, we reduce the system (2.12) to a system of first-order equations. The details of this calculation are presented in the Appendix, and we conclude that (2.12) represents an eighth-order system.

The reduction to a first-order system of equations also shows that the system (2.12) is singular whenever

$$\sigma = \sigma_c = -\frac{\nu_0\left(a_0K_0 + b_0K_0^*\right)}{K_0\left(\xi_0 + \frac{4}{3}\eta_0\right)} - \mathrm{i}k_x u_0. \tag{2.13}$$

These singular points give rise to a continuous spectrum of eigenvalues. The right-hand side of (2.13) is a function of z, so we write the continuous spectrum as $\sigma = \sigma_c(z)$, and there is a singular point of the governing equations for each $z \in (0, \infty)$. However, as each of the steady flow quantities in (2.13) is positive over the entire flow domain, $\mathrm{Re}\,(\sigma_c) \leqslant 0$ and the continuous spectrum does not contribute to instability. An example of the continuous spectrum is shown in figure 1. The previous studies of the linear stability of chute flows (Forterre & Pouliquen 2002; Mitarai & Nakanishi 2004) did not identify the continuous spectrum.

Although the continuous spectrum does not result in instability, its presence can cause numerical difficulties. Since $\mathrm{Re}\,(\sigma_c) \to 0$ as $z \to \infty$, care must be taken to ensure that potentially unstable, discrete eigenvalues with small real part are fully resolved.

2.2. *Boundary conditions*

The system of ordinary differential equations for the normal mode functions is augmented with boundary conditions obtained by linearizing the physical boundary conditions at the planar chute boundary and at the free surface. The linearized boundary conditions of Richman (1988) provide four conditions at the solid boundary which we write in matrix form as

$$\boldsymbol{Q}\frac{\mathrm{d}\boldsymbol{X}}{\mathrm{d}z} + \boldsymbol{R}(k_x, k_y)\boldsymbol{X} = 0 \quad \text{at } z = 0, \tag{2.14}$$

where the components of the 4×5 matrices $\boldsymbol{Q}$ and $\boldsymbol{R}$ are functions of the steady flow solutions, evaluated at the base, as given in the Appendix.

The free surface conditions are determined by making an asymptotic expansion of the linearized governing equations as $z \to \infty$, following Forterre & Pouliquen (2002), as shown in the Appendix. We obtain the asymptotic behaviour of the perturbation velocity components and the perturbation granular temperature:

$$\left.\begin{aligned} \hat{u} &= (U_{10} + U_{11}z)\,\mathrm{e}^{-Kz}, \quad \hat{v} = (V_{10} + V_{11}z)\,\mathrm{e}^{-Kz}, \\ \hat{w} &= (W_{10} + W_{11}z)\,\mathrm{e}^{-Kz}, \quad \hat{T} = T_{10}\mathrm{e}^{-Kz}, \end{aligned}\right\} \tag{2.15}$$

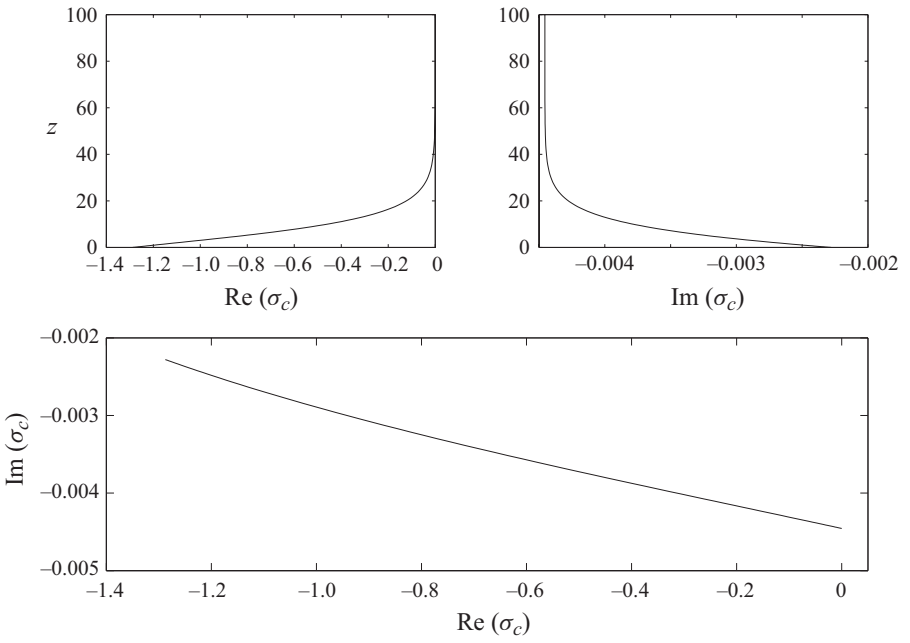

FIGURE 1. The continuous spectrum of eigenvalues $\sigma_c(z)$ obtained from a high temperature steady chute flow with mass flux $Q_0 = 3$, material parameters $e = e_w = 0.8$, $r = 0.6$ and chute slope $\tan\theta = 0.3$, for wavenumbers $k_x = 5 \times 10^{-4}$, $k_y = 0$. The real and imaginary parts of σ_c are plotted as functions of the distance from the chute boundary and together on the complex plane.

for $z \gg 1$, where $K = \sqrt{k_x^2 + k_y^2}$ and

$$V_{10} = -\frac{k_x}{k_y}U_{10} - \frac{\mathrm{i}K}{k_y}W_{10} - \frac{7K}{k_x k_y}U_{11}, \quad V_{11} = \frac{k_y}{k_x}U_{11}, \quad W_{11} = \frac{\mathrm{i}K}{k_x}U_{11}. \tag{2.16}$$

The constants U_{10}, U_{11}, W_{10} and T_{10} remain undetermined. In these results our analysis diverges from the previous studies (Forterre & Pouliquen 2002; Mitarai & Nakanishi 2004) that enforced purely exponential decay (so setting $U_{11} = 0$) and treated V_{10} as an independent constant.

Since the fields and their derivatives vanish at infinity, the physical boundary conditions of vanishing mass flux, momentum flux and energy flux are satisfied. The asymptotic analysis provides four surface conditions to complement the four base boundary conditions imposed on the system. Here our study also differs from the previous contributions (Forterre & Pouliquen 2002; Mitarai & Nakanishi 2004), in which two artificial boundary conditions were added to the system to provide 10 boundary conditions. We have shown that these are unnecessary and that together with the enforced exponential decay, it is possible that the linear system was overprescribed in these earlier studies.

2.3. *Numerical method*

In order to determine those growth rates for which the system above has a solution, we must solve numerically the linear system of ordinary differential equations. The differential eigenproblem can be reduced to a linear eigenproblem by a discretization of the differential operator. The pseudospectral method of discretization is well suited

to eigenvalue problems (Boyd 2000) and is used here to approximate the spatial structure of the normal modes.

As in Part 1, we must transform the governing equations onto a computational domain in order to apply the Chebyshev spectral expansion. The steady-flow computational domain is found from an exponential mapping of the physical space

$$\zeta_0 = \exp(-z/L), \tag{2.17}$$

where the map parameter $L = 2kT_\infty$, for $k \in \mathbb{N}$, is chosen to ensure analyticity in the computational domain. Here, if we transform the physical domain in this way, the perturbation fields are, in general, not analytic as $\zeta \to 0$, as seen from (2.15). Instead, we use a truncation of the semi-infinite physical domain in combination with a two-parameter algebraic mapping, as suggested by Malik (1990) for boundary-layer flow and used in the linear stability analysis of the granular chute flow by Forterre & Pouliquen (2002). The semi-infinite domain is truncated at $z = z_m$ and then transformed to the computational domain, $\zeta_1 \in [0, 1]$, using an algebraic mapping,

$$\zeta_1 = \frac{a - zb}{a - z}, \tag{2.18}$$

for map parameters

$$a = \frac{z_m z_h}{2z_h - z_m}, \qquad b = \frac{z_h}{2z_h - z_m}, \tag{2.19}$$

where $\zeta_1 = 1/2$ at $z = z_h$. This two-parameter mapping therefore allows the clustering of collocation points at the boundary through our choice of z_h.

In order to use the truncation of the semi-infinite physical domain, we need to replace the asymptotic free surface boundary conditions, which are applied in the limit $z \to \infty$, with conditions at the finite truncation point $z = z_m$. The conditions at the truncation point must ensure that the perturbation fields match onto the asymptotic behaviour required as $z \to \infty$. It is sufficient to take the leading-order behaviour by assuming $z_m/T_\infty \gg 1$, so that the volume fraction is sufficiently small for both the steady flow and the perturbation. In our computations, we ensure that z_m is large enough so that $\nu_0(z_m) < 10^{-10}$, which typically results in $z_m/T_\infty > 20$. We construct a simple system of coupled first-order equations that are applied at the truncation point $z = z_m$ to ensure the correct asymptotic decays as $z \to \infty$. The boundary conditions for the velocity components at the truncation point are then given by a simple coupled system of the form

$$\left.\begin{aligned} \hat{u}' + a_1\hat{u} + b_1\hat{v} + c_1\hat{w} &= 0, \\ \hat{v}' + a_2\hat{u} + b_2\hat{v} + c_2\hat{w} &= 0, \\ \hat{w}' + a_3\hat{u} + b_3\hat{v} + c_3\hat{w} &= 0, \end{aligned}\right\} \tag{2.20}$$

where the coefficients are functions of the wavenumbers of the perturbation:

$$\left.\begin{aligned} a_1 &= \frac{8k_x^2 + 7k_y^2}{7K}, & b_1 &= \frac{k_x k_y}{7K}, & c_1 &= \frac{\mathrm{i}k_x}{7}, \\ a_2 &= \frac{k_x k_y}{7K}, & b_2 &= \frac{7k_x^2 + 8k_y^2}{7K}, & c_2 &= \frac{\mathrm{i}k_y}{7}, \\ a_3 &= \frac{\mathrm{i}k_x}{7}, & b_3 &= \frac{\mathrm{i}k_y}{7}, & c_3 &= \frac{6K}{7}, \end{aligned}\right\} \tag{2.21}$$

and are selected such that the general solution of (2.20) has the appropriate asymptotic decay and the required coupling between the velocity components given by (2.15) and

(2.16). For the granular temperature, we simply require

$$\hat{T}' + K\hat{T} = 0, \tag{2.22}$$

at $z = z_m$.

We now seek a spectral approximation to the normal mode amplitude functions, writing, for example

$$\hat{v} = \sum_{j=1}^{M+1} \hat{v}_j T_{j-1}(2\zeta_1 - 1), \tag{2.23}$$

and similarly for $\hat{u}, \hat{v}, \hat{w}, \hat{T}$, where the arguments of the Chebyshev polynomials introduce a further mapping of the computational domain onto the domain of the Chebyshev polynomials. On inserting the spectral expansions into the ordinary differential equations for the normal modes and the boundary conditions at the base and truncation point, after the appropriate transformation of derivatives into the computational domain, we obtain a system of algebraic equations for the spectral expansion coefficients.

The $5M+5$ spectral expansion coefficients are determined by enforcing the algebraic equations at a subset of the $M + 3$ collocation points, made up of the roots of $T_{M+1}(2\zeta_1 - 1) = 0$ together with the base boundary $\zeta_1 = 1$ and the truncation point $\zeta_1 = 0$. The linear differential eigenproblem is reduced to a generalized eigenvalue problem of the form

$$\boldsymbol{A}\boldsymbol{x} = \sigma \boldsymbol{B}\boldsymbol{x}, \tag{2.24}$$

where the eigenvalue σ is the growth rate of the perturbation, and the eigenvector $\boldsymbol{x}$ is the vector of spectral expansion coefficients. The matrices $\boldsymbol{A}$ and $\boldsymbol{B}$ are the discretized governing equations evaluated at the collocation points, together with the four base boundary conditions and the four conditions at the truncation point. The matrices $\boldsymbol{A}$ and $\boldsymbol{B}$ are of dimension $(5M + 5) \times (5M + 5)$, are complex-valued and depend on the wavenumbers of the perturbation. In addition, since the boundary conditions are time independent, the eigenvalue does not appear in the boundary conditions. Therefore the matrix $\boldsymbol{B}$ is singular and so the generalized problem cannot be reduced to a standard eigenvalue problem by inverting $\boldsymbol{B}$. The generalized eigenvalue problem can be solved numerically using the standard QZ-algorithm for complex matrices (Moler & Stewart 1973; Anderson *et al.* 1999), which computes the complete spectrum of eigenvalues and the corresponding eigenvectors.

It is well known that the pseudospectral discretization of the differential eigenproblem produces spurious eigenvalues (Boyd 2000). These can be located by making a second approximation with a higher truncation. The locations of the spurious modes are sensitive to the spectral truncation, whereas the physical modes remain in place. In addition, the physical modes are well resolved, so that the spectral expansion coefficients (given in the eigenvector) show a characteristic exponential decay. The spurious modes are not well resolved, so decay of the components of the eigenvector can be used to confirm those physical eigenvalues.

Although the QZ-algorithm provides the whole spectrum of eigenvalues, the computational cost increases dramatically for large matrices (the number of operations increases with n^3 for $n \times n$ matrices Golub & Van Loan 1989). Typically, we take a truncation of $M = 100$, although it is often necessary to increase this value when considering the linear stability of the dense steady solutions on the low temperature branch where expansions of degree $M = 500$ may be required to obtain

convergence. The second approximation is taken to be 20 % larger. As we seek the stability of the steady flows over a large range of wavenumbers, we also make use of an inverse iteration method to avoid excessive computational expense (Golub & Van Loan 1989). Unlike the QZ-algorithm, inverse iteration is a local method with only a single eigenvalue and eigenvector calculated. We therefore use the QZ-algorithm on a coarse grid of wavenumbers, with the inverse iteration filling in, using the dominant eigenvalue and its corresponding eigenvector at a neighbouring wavenumber as the initial guess. Care must be taken to ensure the dominant eigenvalue is calculated by the local iteration, particularly at mode crossings where it is necessary to employ the QZ-algorithm on the fine mesh of wavenumbers.

In order to estimate the decrease in the time of computation when the iterative procedure is employed, we calculated the most unstable mode for 10 wavenumbers using the QZ-algorithm and the inverse iteration with a single QZ initiation. With a truncation of $M = 100$ the inverse iteration was found to accurately calculate the dominant eigenvalue, and the time required for the calculation was reduced by a factor of seven when using the iterative method rather than the QZ-algorithm alone. The speed-up in the calculation increases as the truncation increases, with a factor 10 reduction in computation time if $M = 300$. The calculation was performed on a 2.8 GHz machine and the time taken when using the QZ-algorithm alone was 7 min 21 s when $M = 100$, rising to 4 h 18 min 38 s when $M = 300$. In comparison, if iteration is employed, the calculation is completed in 1 min when $M = 100$ and 25 min 44 s when $M = 300$. The significant reduction in computational time when iteration is employed is clearly beneficial when considering a large set of wavenumbers where only the dominant eigenvalue is required.

3. Results

3.1. *Typical eigenspectrum*

Figure 2 shows a typical eigenspectrum, here taken from the high temperature steady flow with mass flux $Q_0 = 3$, material parameters $e = e_w = 0.8$, $r = 0.6$ and chute slope $\tan\theta = 0.3$ (see figure 2, Part 1). The perturbation wavenumbers are $k_x = 5 \times 10^{-4}$, $k_y = 0$. Many of the discrete eigenvalues in the portion of complex plane shown are well converged. However, there is a 'balloon' of poorly converged eigenvalues surrounding the analytically determined continuous spectrum. These eigenvalues converge extremely slowly on increasing the truncation of the pseudospectral series. We note that the dominant eigenvalue, which here has positive real part, lies in close proximity to this balloon, which can interfere in the calculation of this eigenvalue unless a sufficiently large truncation of the pseudospectral series is employed. With sufficient resolution the poorly converged eigenvalues remain in the stable half-plane and unstable eigenvalues can be determined.

3.2. *Linear stability of multiple steady flow solutions*

In Part 1, we demonstrated the existence of multiple flow solutions for a fixed mass flux of material. Here we consider a particular choice of flow parameters that give rise to multiple solutions, taking $e = e_w = 0.8$, $r = 0.6$ and $\tan\theta = 0.3$. The three possible solutions with mass flux $Q_0 = 3$ are shown in Part 1 and are described as the high temperature, mid-temperature and low temperature flows. We consider now the linear stability characteristics of these three steady flow solutions.

The growth rates $\mathrm{Re}(\sigma)$ for the most unstable mode (i.e. the supremum of the discrete set of eigenvalues) for the three steady solutions with $Q_0 = 3$ are shown

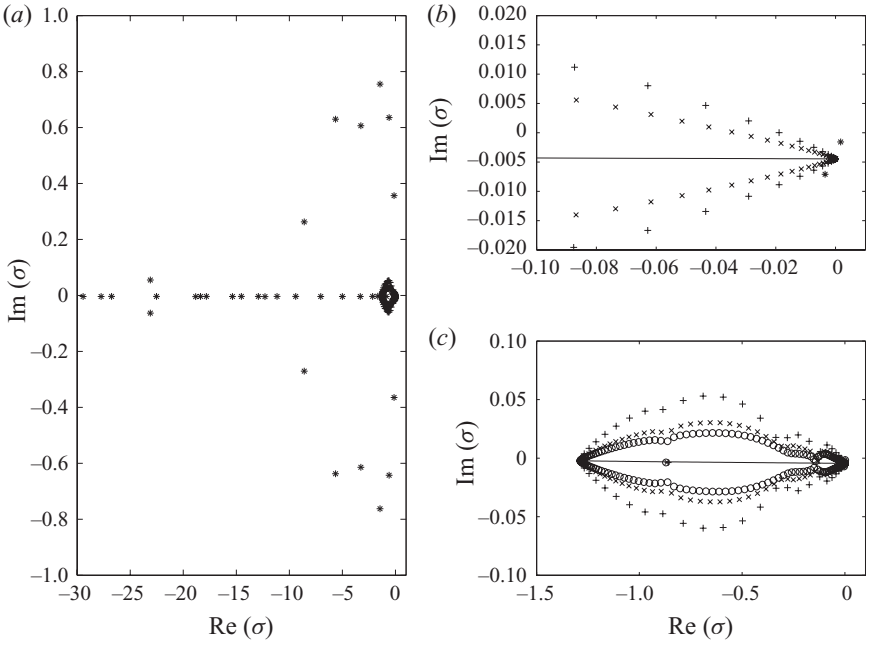

FIGURE 2. The spectrum of eigenvalues obtained from the normal mode, linear stability analysis of the high temperature steady chute flow with mass flux $Q_0 = 3$ ($e = e_w = 0.8$, $r = 0.6$, $\tan\theta = 0.3$), with wavenumbers $k_x = 5 \times 10^{-4}$, $k_y = 0$. (*a*) Eigenvalues calculated with pseudospectral truncations of $M = 100$ (+) and $M = 200$ (×). (*b*) Magnification of the eigenspectrum showing the dominant eigenvalue and the analytically determined continuous spectrum (—). (*c*) The balloon of poorly resolved eigenvalues surrounding the continuous spectrum shrinks slowly on increasing the pseudospectral approximation with $M = 100$ (+), $M = 200$ (×) and $M = 300$ (○).

in figure 3, as functions of the perturbation wavenumbers k_x and k_y. The most unstable mode for the high temperature flow has wavenumbers $k_x = 0$, $k_y = 0.0100$ and growth rate $\sigma \approx 0.00397$. Thus, the fastest-growing mode is a purely cross-slope perturbation, with a wavelength of the order of 600 particle diameters. The contour plot for the mid-temperature flow is qualitatively similar to that of the high temperature flow, with a region of instability for both $k_x > 0$ and $k_y > 0$, and with the most unstable mode corresponding to a purely cross-slope perturbation. The range of unstable purely cross-slope ($k_x = 0$) wavenumbers is also similar, but the corresponding range for purely downslope ($k_y = 0$) wavenumbers is reduced. The most unstable mode for the mid-temperature flow has wavenumbers $k_x = 0$, $k_y = 0.0125$, a purely cross-slope perturbation, and growth rate $\sigma \approx 0.00102$. The dispersion relation for the low temperature flow is qualitatively different from those for the high and mid-temperature flows. We again see exponentially growing modes for both $k_x > 0$ and $k_y > 0$ with the regions of instability extending to similar values of k_x and k_y, but the purely downslope perturbations generally have fastest growth. Indeed, the most unstable mode is a purely downslope ($k_y = 0$) perturbation with wavenumber $k_x = 0.011$. The wavelength of the most unstable mode is then comparable to the wavelengths of the most unstable modes for the high and mid-temperature modes. For the low temperature flow the most unstable mode has $\sigma \approx 0.00727$–0.0119i and so the exponential growth rate is of the same order of magnitude as the growth rates

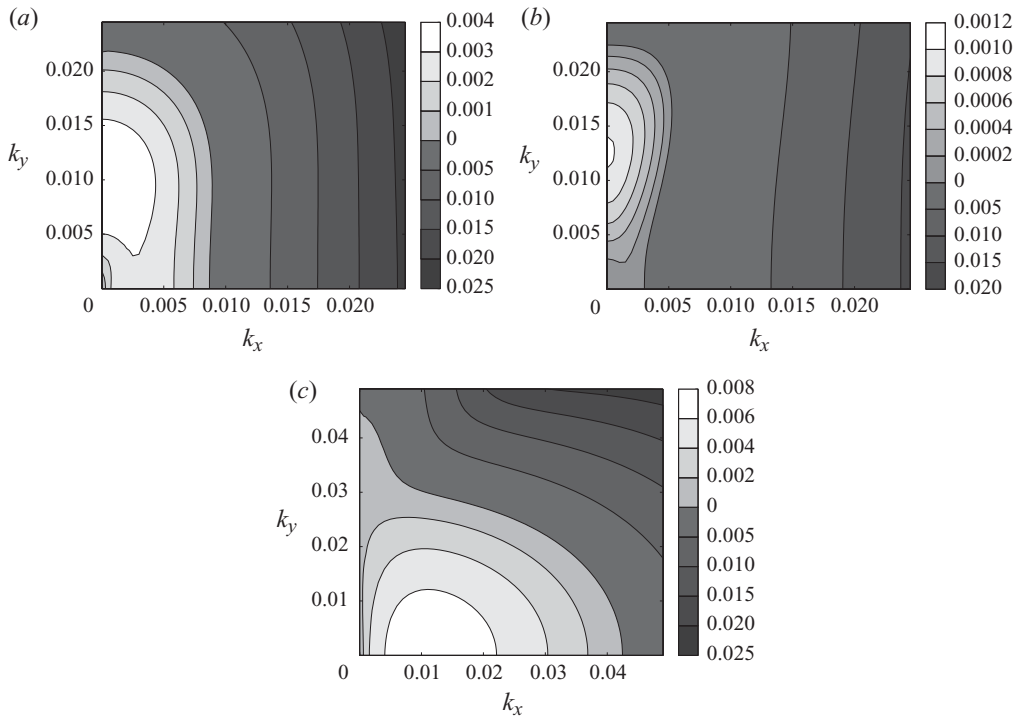

FIGURE 3. Contours of the maximum growth rate $\mathrm{Re}(\sigma)$, as a function of the perturbation wavenumbers k_x, k_y, for (*a*) the high temperature, (*b*) mid-temperature and (*c*) low temperature steady chute flows with mass flux $Q_0 = 3$ ($e = e_w = 0.8$, $r = 0.6$, $\tan\theta = 0.3$). Note varying axes and colour scales.

for the high and mid-temperature flows, and additionally the downslope perturbation propagates in time relative to the steady flow.

In figure 4 we plot the eigenfunctions corresponding to the most unstable perturbations of the three steady chute flows. For clarity we have plotted the eigenfunctions to a height much smaller than the truncation height, given by z_m in (2.19), used in the numerical solution. The volume fraction perturbation is localized at the base boundary and the exponential decay of the volume fraction perturbation away from the base is clear, whereas the remaining fields decay more slowly since their asymptotic profile is determined by the wavenumber of the perturbation, which is smaller than the far-field granular temperature of the corresponding steady flow. Note that the most unstable mode for the low temperature steady flow is a purely downstream perturbation and there is no cross-slope velocity component for this perturbation. For the high and mid-temperature steady flows the perturbation has a three-dimensional velocity field, with the cross-slope velocity component out-of-phase with the downslope and vertical components.

The perturbed fields can be reconstructed from the eigenfunctions by introducing the sinusoidal downslope and cross-slope variations. The instantaneous fields for the three steady flows are shown in figure 5 over two wavelengths. The structure of the perturbations to the high and mid-temperature steady flows is broadly similar, with the granular temperature perturbation largest in locally dilute regions of the flow

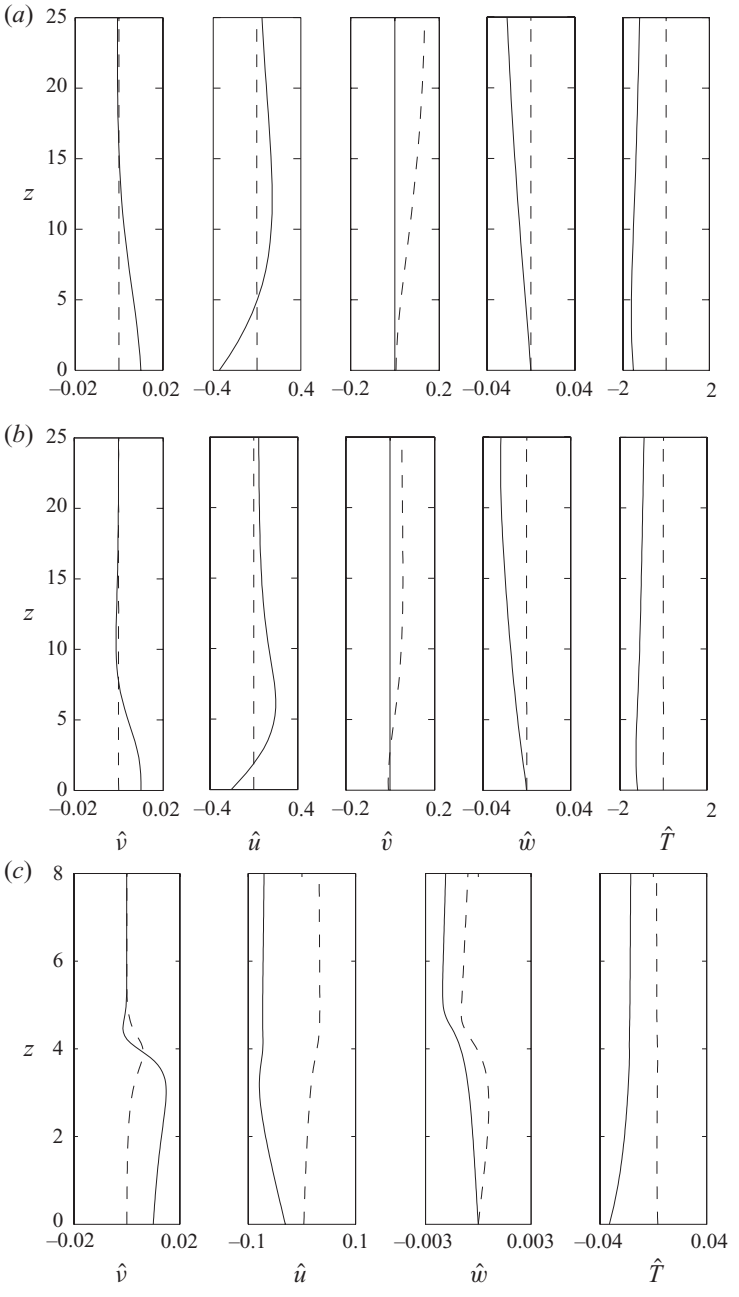

FIGURE 4. Eigenfunctions of the most unstable perturbations to (*a*) the high temperature ($k_x = 0$, $k_y = 0.01$), (*b*) mid-temperature ($k_x = 0$, $k_y = 0.0125$) and (*c*) low temperature ($k_x = 0.011$, $k_y = 0$) steady chute flows with mass flux $Q_0 = 3$ ($e = e_w = 0.8$, $r = 0.6$, $\tan\theta = 0.3$). The real part (—) and imaginary part (– –) of the eigenfunctions are shown.

(where the volume fraction perturbation is negative). The downslope (u_1) and vertical (w_1) perturbation velocity components are also largest in dilute regions, but the cross-slope velocity is out-of-phase with the other velocity components by $\pi/2$. The high and mid-temperature perturbations are stationary, since $\mathrm{Im}(\sigma) = 0$. In contrast,

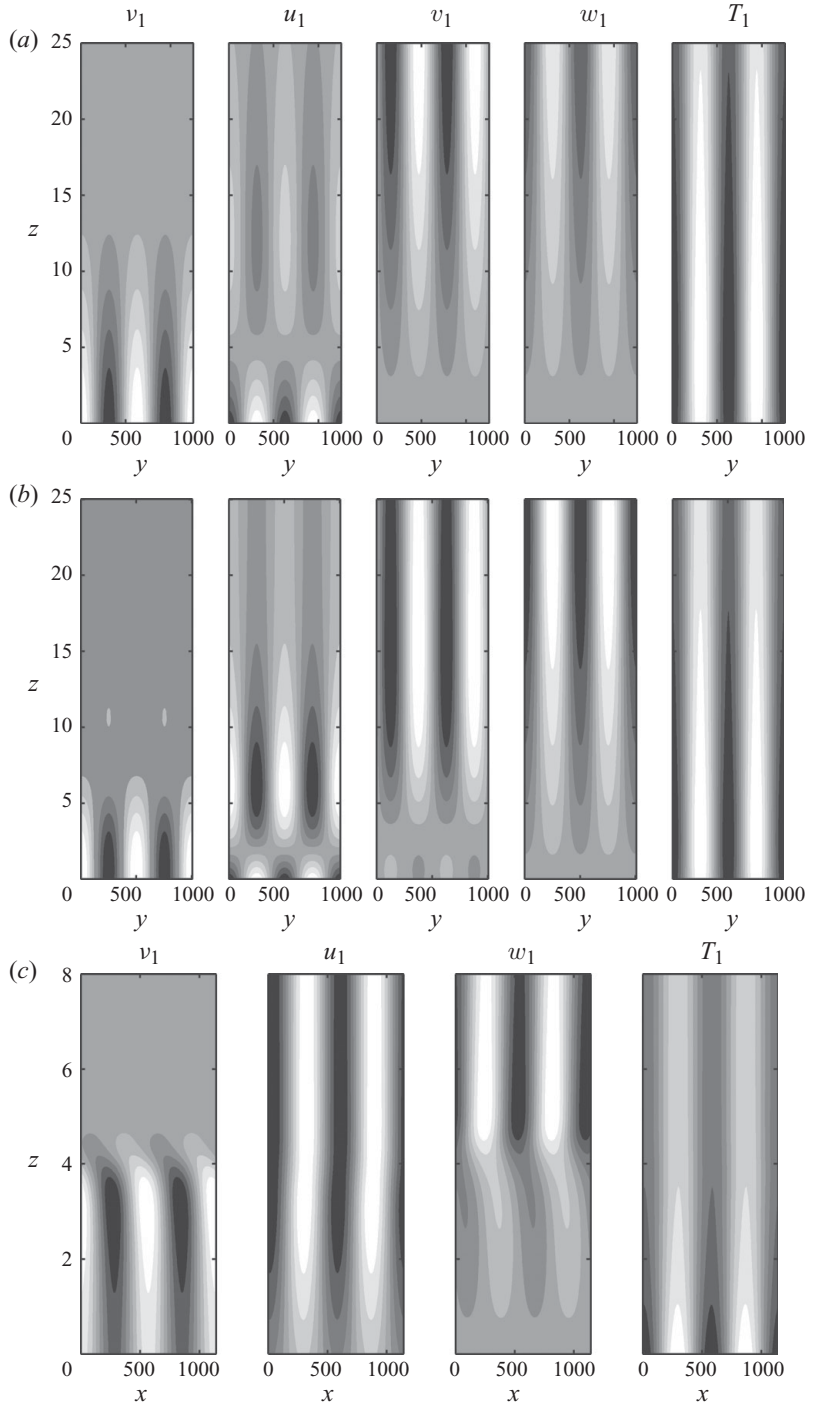

FIGURE 5. Contours of the most unstable perturbations to (*a*) the high temperature, (*b*) mid-temperature and (*c*) low temperature steady chute flows with mass flux $Q_0 = 3$. The grey scale colouring is white for the most positive value and black for the most negative value. In (*a*) and (*b*) $k_x = 0$ and a slice has been taken across the chute slope, whereas in (*c*) $k_y = 0$ and we take a downslope slice.

the downslope perturbation for the low temperature steady flow is a propagating instability, so the fields are in motion relative to the steady flow. The wavelengths of the perturbations to the three steady flows are similar, around 500 particle diameters.

The nature of the instabilities can be elucidated by examining the transport of grains by the perturbation fields. The local mass flux of the perturbation is defined as the vector $\boldsymbol{Q_1} = (Q_x, Q_y, Q_z)$, where

$$Q_x = \nu_0 u_1 + \nu_1 u_0, \qquad Q_y = \nu_0 v_1, \qquad Q_z = \nu_0 w_1. \tag{3.1}$$

In figure 6 we plot vectors of the local perturbation mass flux together with perturbation volume fraction contours for the most unstable mode for each of the three steady chute flows. Although the structure of the perturbations for the high and mid-temperature steady flows is qualitatively similar, as shown in figure 5(*a, b*), the local transport of grains in these flows is distinctly different. For the high temperature steady flow grains are transported out of locally dilute regions, where the volume fraction perturbation is negative, into locally dense regions. Thus, the density contrast is enhanced and the perturbation grows because of the clustering of grains. In contrast, for the mid-temperature steady flow the perturbation results in a vortical structure to the grain transport, with two counter-rotating vortices in each wavelength. Vortex-forming perturbations were also found by Forterre & Pouliquen (2002). The vortices form here because of a small cross-slope slip velocity at the base boundary that is not present for the most unstable mode of the high temperature steady flow. However, it is possible to obtain vortex-forming modes for the high temperature steady flow at different wavenumbers. The perturbation to the low temperature steady flow is a clustering instability, with a transport of grains from locally dilute to locally dense regions. No vortex-forming perturbations have been found for the low temperature steady flow.

3.3. *Linear stability characteristics on macroscopic flow curves*

We consider now the linear stability of steady flows when characterized by macroscopic, depth-integrated variables. The stability analysis for the three steady solutions with mass flux $Q_0 = 3$ ($e = e_w = 0.8$, $r = 0.6$, $\tan\theta = 0.3$) shows that each of the flows is linearly unstable to small perturbations, and we may ask whether any of the steady flow solutions are linearly stable?

The linear stability of the steady flows along the Q–h curve for the material parameters $e = e_w = 0.8$, $r = 0.6$ and chute slope $\tan\theta = 0.3$ is shown in figure 7. A region of linearly stable flows is found on the mid-temperature branch, occupying a relatively small portion of the curve. The dilute, high temperature flows and the dense, low temperature flows are found to be linearly unstable. The contours of the maximum growth rate for selected steady flows along the Q–h curve demonstrate the cross-slope instability at high temperature and downslope instability at low temperature. The fastest growth rate in this set occurs for the steady flow with the lowest granular temperature (the low temperature flow with $Q_0 = 3$).

In figure 7(*a*) we have indicated those steady flows for which a density inversion is found. For classical fluids, relatively dense flows overlying dilute flows are often gravitationally unstable. For this reason, density inversions have been proposed as a cause of instability (Forterre & Pouliquen 2001, 2002). However, we see from figure 7 that a density inversion in the steady flows is neither a necessary nor sufficient condition for instability; there are steady flows with density inversions that are

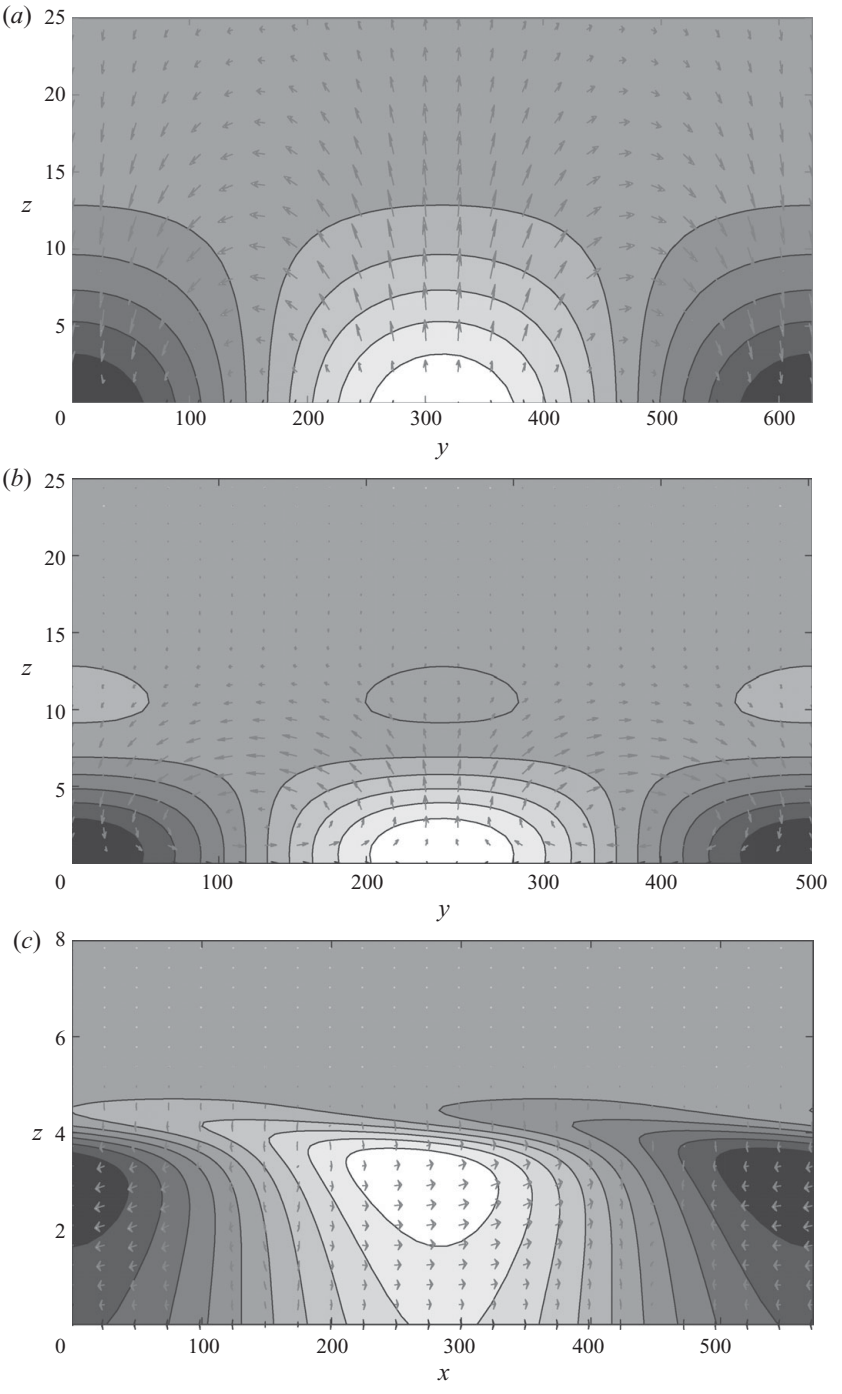

FIGURE 6. Local mass flux vectors and volume fraction contours for (*a*) the high temperature, (*b*) mid-temperature and (*c*) low temperature steady chute flows with mass flux $Q_0 = 3$ ($e = e_w = 0.8$, $r = 0.6$, $\tan\theta = 0.3$). For the cross-slope perturbations in (*a*) and (*b*) the vectors have components (Q_y, Q_z), whereas for the downslope perturbation in (*c*), the vectors are (Q_x, Q_z). Shading indicates the perturbation to the volume fraction field, with dark regions being locally dense and light regions locally dilute.

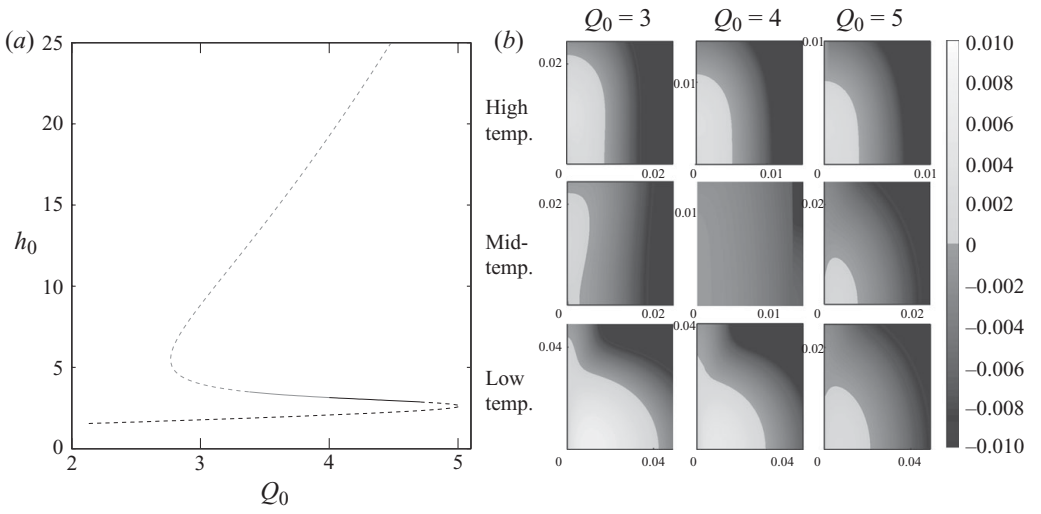

FIGURE 7. (*a*) Linear stability of steady chute flows on a macroscopic Q–h curve. Material parameters are set at $e = e_w = 0.8$, $r = 0.6$ and the chute slope is $\tan\theta = 0.3$. Linearly stable (—) and unstable (– –) regions are indicated, and a heavy line shows flows for which the steady solution exhibits a density inversion. (*b*) Contours of the maximum growth rate as a function of the wavenumbers k_x and k_y for selected steady flows along the Q–h curve.

linearly stable, and there are linearly unstable flows with no density inversion. This latter finding was recognized by Forterre & Pouliquen (2002), who found linearly unstable, non-inverted flows that are relatively dilute and deep, as we obtain here.

The effect of changing the slope inclination is shown in figure 8, where the linear stability of steady flows is assessed along several macroscopic flow curves. The material parameters are fixed as $e = e_w = 0.8$ and $r = 0.6$. For gently inclined chutes, with $\tan\theta \leqslant 0.28$, all steady flows are linearly unstable. A region of linear stability is found for inclinations with $0.29 \leqslant \tan\theta \leqslant 0.32$, and this region always occurs on the mid-temperature solution branch of the Q–h curve. The length of the linearly stable region grows with increasing inclination until there is an abrupt change and, on chutes with slopes $\tan\theta \geqslant 0.33$, the steady flows are again always linearly unstable. This transition on relatively steep slopes coincides with a change in the structure of the Q–h curves, from curves where three solutions for a fixed mass flux are possible to curves where two solutions are always found for a specified mass flux. The transition between density-inverted steady solutions and monotonic density profiles is not seen to correlate with the linear stability of the steady flows.

4. Discussion

4.1. *Comparison with previous studies*

Our investigation of the linear stability of steady chute flows has identified three qualitatively different instability modes: two cross-slope instabilities, one forming counter-rotating vortices, the other a non-vortex-forming clustering of grains, and a downslope, non-vortex-forming clustering. The vortex-forming cross-slope instability has previously been identified by Forterre & Pouliquen (2002), and the downslope instability by Mitarai & Nakanishi (2004). The cross-slope clustering instability

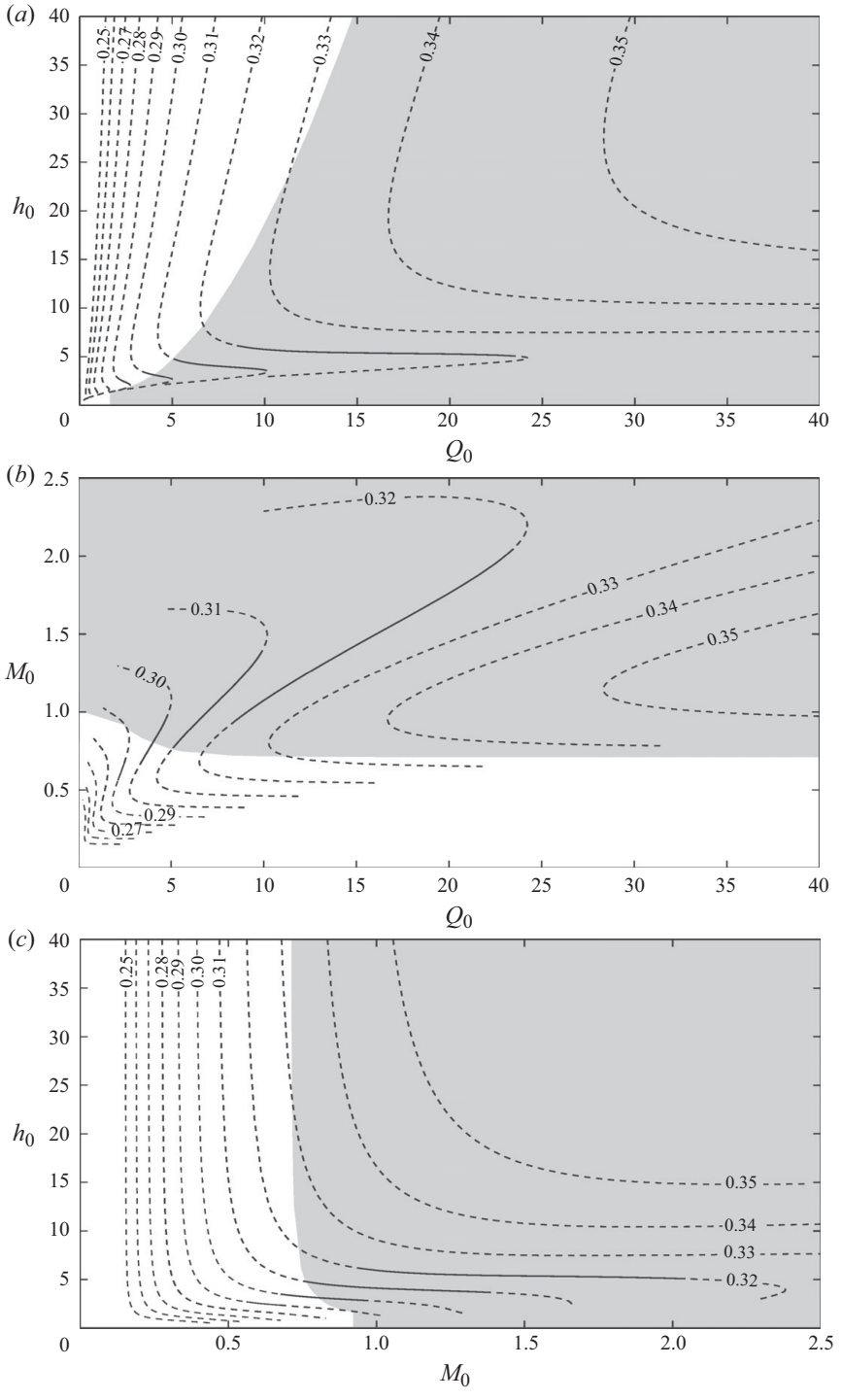

FIGURE 8. Linear stability of steady chute flows on macroscopic curves as the chute slope is varied with $\tan\theta \in [0.25, 0.35]$, as indicated. Material parameters are set at $e = e_w = 0.8$, $r = 0.6$. Linearly stable (—) and unstable (– –) regions are found using a Chebyshev pseudospectral stability analysis coupled with a pseudospectral continuation of the steady flow solutions. The shaded regions indicate flows for which the steady solution exhibits a density inversion.

appears to be novel. Our three-dimensional analysis shows that these instabilities can coexist for a fixed set of material parameters and a fixed chute inclination.

In the examples seen above, the most unstable perturbation is two-dimensional (i.e. either purely cross-slope, with $k_x = 0$, $k_y > 0$, or purely downslope, with $k_x > 0$, $k_y = 0$). However, it is possible to find steady solutions for which the most unstable mode has both $k_x > 0$ and $k_y > 0$. These steady solutions typically occur on steep slopes, with $\tan\theta \geqslant 0.33$ for material parameters $e = e_w = 0.8$, $r = 0.6$, and at low temperature. The resulting perturbations are a combination of downslope clustering with cross-slope vortices, with the wavenumber of the cross-slope perturbation an order of magnitude larger than the downslope perturbation. The instabilities found above are long wavelength, with wavelengths of several hundred grain diameters. This is in contrast with the instabilities calculated by Forterre & Pouliquen (2002), where the wavelengths are typically of around 30 grain diameters.

It is not possible to compare the solutions of the continuum model with the flows observed in the experiments of Forterre & Pouliquen (2001) since we cannot achieve steady flows from the continuum model for the steep slopes used in the experiments, where $\tan\theta = 0.78$. This suggests that either the experimental flows are not fully collisional, or the simple kinetic theory of Lun *et al.* (1984) is not able to describe these flows and an extended kinetic theory is required, perhaps accounting for frictional interactions, or perhaps the experimental flows are not fully developed, although this is unlikely in view of the large apparatus used. As the kinetic theory of Lun *et al.* (1984) is derived for monodisperse spherical grains, and the experiment of Forterre & Pouliquen (2001) was conducted with grains of sand, we do not expect the kinetic continuum model to fully describe all aspects of the observations.

When examining the linear stability of steady solutions in parameter space, we find that linearly stable steady solutions exist for only a limited range of inclination angles. If the chute slope is sufficiently gentle or sufficiently steep, we are unable to find linearly stable steady flows. This is in contrast to the results of Forterre & Pouliquen (2002), who find an inclination angle below which all steady flows are linearly stable to cross-slope perturbations. However, the instabilities on the relatively gentle slopes which we find here occur for purely cross-slope perturbations with $k_x = 0$. The instabilities we find on the gently inclined chutes occur at long wavelength, and at these small wavenumbers the contrast between purely exponential decay of the perturbation fields, as employed by Forterre & Pouliquen (2002), and the far-field behaviour given in (2.15) is enhanced. Furthermore, at small wavenumbers the balloon of poorly converged eigenvalues surrounding the continuous spectrum extends close to the unstable mode and the unstable mode can be lost within the balloon unless a sufficiently large truncation of the pseudospectral series is taken. The discrepancy between our results and those of Forterre & Pouliquen (2002) may be due to insufficient numerical resolution in this earlier study.

4.2. *Implications for the instability mechanism*

The stability analysis performed by Forterre & Pouliquen (2002) suggests two physical processes that lead to instability in the steady chute flow: (i) density inversion in the underlying steady flow and (ii) inelastic clustering.

The density inversion of the steady flow is due to the production of fluctuation energy at the base boundary, which leads to a heating of the interior and reduces the density at the base, while collisions in the flow dissipate this energy and can cause an increase in the density. A perturbation to a density-inverted steady flow

may disrupt the energy balance in such a way that the dilute flow near the base cannot support the dense fluid above, and the gravitational body force causes an overturning. This process is in some ways analogous to the classical Rayleigh–Bénard instability (Drazin & Reid 1981; Forterre & Pouliquen 2002), where a fluid layer heated from below becomes unstable above a critical Rayleigh number and a convective overturning of fluid is initiated. However, for the granular layer it is not possible to define a control parameter analogous to the Rayleigh number (Forterre & Pouliquen 2002). In addition, the heating of the granular layer at the base is due to the motion of grains relative to the bumpy boundary and not by an external energy source as for the fluid layer, and so a perturbation to the steady granular flow alters the supply of fluctuation energy from the base. The density-inverted steady flows are also dissipative in the interior, so fluctuation energy produced at the base may be lost in the interior, whereas the energy input from the heated base is conserved in the fluid layer and lost only at boundaries of the domain.

Inelastic clustering results from the dissipation of fluctuation energy in inelastic collisions and has been identified as a robust instability mechanism in molecular dynamics simulations of granular assemblies (e.g. Hopkins & Louge 1991; Goldhirsch & Zanetti 1993; McNamara & Young 1994; Liss *et al.* 2002), and has been observed in linear stability analysis of sheared granular systems (see Alam & Nott 1998; Alam 2006). A perturbation to a steady granular flow, in which there is a balance between the production and dissipation of fluctuation energy, which locally increases the density in some region, causes a local increase in the rate of collisions. The increased dissipation cools the locally dense region, causing a temperature gradient and a resulting transport of heat into this region. As the heat is carried as fluctuation energy of the grains, a transport of heat into locally dense regions implies that energetic grains are transported from locally dilute regions into locally dense regions. Here collisions with less energetic grains result in a dissipation of energy. Thus, grains are carried into the locally dense region. If this energy transport is sufficient to balance the increased dissipation, the perturbation will not grow, otherwise the additional energy is dissipated and the density is further increased, resulting in the formation of dense clusters of grains.

Forterre & Pouliquen (2002) provide evidence that each of these mechanisms are capable of causing the loss of stability in a granular chute flow and suggest that the gravitationally induced overturning is the dominant mechanism in the parameter regimes where density inversions are found, and the instability results in the formation of longitudinal vortices. On the other hand, Mitarai & Nakanishi (2004), who take downslope perturbations to a steady chute flow, suggest that inelastic clustering is dominant and results in long-wavelength density waves.

Our analysis supports inelastic clustering as the dominant mechanism, although we cannot discount the gravitational instability when there is a density inversion of the steady solution. We have seen that cross-slope, vortex-forming instabilities are present when the steady flow has a monotonic density profile, so a density inversion is not necessary for overturning to occur. Furthermore, the most rapidly growing perturbations to some density-inverted steady flows are long wavelength, downslope perturbations with no vortices in the interior. The study of the linear stability characteristics along macroscopic flow curves demonstrates that the regions of linear stability do not correlate with the existence of density-inverted steady flows. Finally, the unstable perturbations we find are most often long-wavelength perturbations.

5. Conclusion

In Part 1 of this paper, we developed a continuum model of rapid granular chute flows and investigated the character of steady solutions. Here we have performed a linear stability analysis of some of these steady flows. Our analysis has extended those of Forterre & Pouliquen (2002) and Mitarai & Nakanishi (2004), by allowing fully three-dimensional perturbations to the steady state, and corrects the free surface boundary conditions that were overspecified in these previous studies. We have shown the existence of a continuous spectrum of eigenvalues, which lies close to the origin in the complex plane and results in a balloon of poorly resolved eigenvalues that may obscure unstable eigenvalues. We therefore require high accuracy in the computation of the steady solution and in the solution of the eigenproblem we obtain from the normal mode analysis. The Chebyshev pseudospectral method developed in Part 1 to compute the steady solutions provides a highly accurate polynomial approximation of the steady solution fields.

We have demonstrated the existence of three qualitatively different forms of instability: a cross-slope, vortex-forming perturbation; a cross-slope, clustering (non-vortex-forming) perturbation; and a downslope clustering perturbation that propagates against the steady flow. Each of these can be the most rapidly growing perturbation for different steady flows.

Our study of the steady flows in Part 1 showed families of solutions for fixed flow parameters, and we traced curves of the macroscopic, depth-integrated centre of mass h as the mass flux Q was varied. In certain regions of parameter space, multiple steady solutions were found for a fixed mass flux of material. An examination of the linear stability characteristics for steady flows along these macroscopic flow curves shows that a region of linear stability is confined to the mid-temperature branch and exists only for a limited range of inclination angles. Outside this small region, all steady flows are found to be unstable.

The results of our analysis support the inelastic clustering mechanism as the dominant destabilizing influence, and although the Rayleigh–Bénard-like mechanism for density-inverted steady flows has been shown to cause instability (Forterre & Pouliquen 2002), we show that there is no correlation between the existence of density-inverted steady flows and linear instability. Indeed, we find monotonic steady flows that are linearly unstable to vortex-forming cross-slope perturbations, density-inverted steady flows for which the most unstable mode does not result in overturning, and steady flows with a density inversion that are linearly stable.

Through our analysis of rapid granular flows on inclined chutes, we have developed a methodology for studying granular flows in more general settings. The pseudospectral method employed in Part 1 to calculate steady solutions, and developed here to determine the linear stability of these steady flows, could be adapted to study granular flows in other geometries or with alternative constitutive relations. For example, the basic kinetic theory used here has been extended systematically to include Burnett order terms (Sela & Goldhirsch 1998; Kumaran 2008), and phenomenologically to account for the development of enduring contacts between grains (Jenkins 2007) in an attempt to model rapid granular flows at high density. We anticipate that the techniques developed in this analysis could be used to analyse the predictions of these more elaborate models of granular flow.

M.J. Woodhouse is grateful to the EPSRC for funding through a doctoral training grant. We thank Richard Kerswell and James Jenkins for informative discussions.

Appendix. Details of the linear stability analysis

A.1. *Linearization of governing equations*

When the perturbation from the steady flow solution is small, the system of partial differential equations can be linearized. The linearized mass conservation equation is

$$\frac{\partial \nu_1}{\partial t} + u_0 \frac{\partial \nu_1}{\partial x} + \nu_0 \left(\frac{\partial u_1}{\partial x} + \frac{\partial v_1}{\partial y} + \frac{\partial w_1}{\partial z} \right) + w_1 \frac{\mathrm{d}\nu_0}{\mathrm{d}z} = 0. \tag{A 1}$$

Linearization of the momentum conservation equation gives components in the downslope direction,

$$\begin{aligned} \nu_0 \left(\frac{\partial u_1}{\partial t} + u_0 \frac{\partial u_1}{\partial x} + w_1 \frac{\mathrm{d}u_0}{\mathrm{d}z} \right) &= \nu_1 \tan\theta \\ &- \frac{\partial}{\partial x} \left(a_0 \nu_1 + b_0 T_1 - \left(\xi_0 + \frac{4}{3}\eta_0 \right) \frac{\partial u_1}{\partial x} - \left(\xi_0 - \frac{2}{3}\eta_0 \right) \frac{\partial v_1}{\partial y} - \left(\xi_0 - \frac{2}{3}\eta_0 \right) \frac{\partial w_1}{\partial z} \right) \\ &- \frac{\partial}{\partial y} \left(-\eta_0 \frac{\partial u_1}{\partial y} - \eta_0 \frac{\partial v_1}{\partial x} \right) - \frac{\partial}{\partial z} \left(-\eta_0 \frac{\partial u_1}{\partial z} - \eta_0 \frac{\partial w_1}{\partial x} - c_0 \frac{\mathrm{d}u_0}{\mathrm{d}z} \nu_1 - d_0 \frac{\mathrm{d}u_0}{\mathrm{d}z} T_1 \right), \end{aligned} \tag{A 2}$$

the cross-slope direction,

$$\begin{aligned} \nu_0 \left(\frac{\partial v_1}{\partial t} + u_0 \frac{\partial v_1}{\partial x} \right) &= -\frac{\partial}{\partial x} \left(-\eta_0 \frac{\partial v_1}{\partial x} - \eta_0 \frac{\partial u_1}{\partial y} \right) \\ &- \frac{\partial}{\partial y} \left(a_0 \nu_1 + b_0 T_1 - \left(\xi_0 - \frac{2}{3}\eta_0 \right) \frac{\partial u_1}{\partial x} - \left(\xi_0 + \frac{4}{3}\eta_0 \right) \frac{\partial v_1}{\partial y} - \left(\xi_0 - \frac{2}{3}\eta_0 \right) \frac{\partial w_1}{\partial z} \right) \\ &- \frac{\partial}{\partial z} \left(-\eta_0 \frac{\partial v_1}{\partial z} - \eta_0 \frac{\partial w_1}{\partial y} \right), \end{aligned} \tag{A 3}$$

and the normal direction,

$$\begin{aligned} \nu_0 \left(\frac{\partial w_1}{\partial t} + u_0 \frac{\partial w_1}{\partial x} \right) &= -\nu_1 - \frac{\partial}{\partial x} \left(-\eta_0 \frac{\partial w_1}{\partial x} - \eta_0 \frac{\partial u_1}{\partial z} - c_0 \frac{\mathrm{d}u_0}{\mathrm{d}z} \nu_1 - d_0 \frac{\mathrm{d}u_0}{\mathrm{d}z} T_1 \right) \\ &- \frac{\partial}{\partial y} \left(-\eta_0 \frac{\partial w_1}{\partial y} - \eta_0 \frac{\partial v_1}{\partial z} \right) \\ &- \frac{\partial}{\partial z} \left(a_0 \nu_1 + b_0 T_1 - \left(\xi_0 - \frac{2}{3}\eta_0 \right) \frac{\partial u_1}{\partial x} - \left(\xi_0 - \frac{2}{3}\eta_0 \right) \frac{\partial v_1}{\partial y} - \left(\xi_0 + \frac{4}{3}\eta_0 \right) \frac{\partial w_1}{\partial z} \right). \end{aligned} \tag{A 4}$$

Finally, linearization of the energy conservation equation gives

$$\begin{aligned} \frac{3}{2}\nu_0 \left(\frac{\partial T_1}{\partial t} + u_0 \frac{\partial T_1}{\partial x} + w_1 \frac{\mathrm{d}T_0}{\mathrm{d}z} \right) &= -p_0 \left(\frac{\partial u_1}{\partial x} + \frac{\partial v_1}{\partial y} + \frac{\partial w_1}{\partial z} \right) + \eta_0 \frac{\mathrm{d}u_0}{\mathrm{d}z} \frac{\partial u_1}{\partial z} \\ &+ \left(\eta_0 \frac{\partial w_1}{\partial x} + \eta_0 \frac{\partial u_1}{\partial z} + c_0 \frac{\mathrm{d}u_0}{\mathrm{d}z} \nu_1 + d_0 \frac{\mathrm{d}u_0}{\mathrm{d}z} T_1 \right) \frac{\mathrm{d}u_0}{\mathrm{d}z} + \eta_0 \frac{\mathrm{d}u_0}{\mathrm{d}z} \frac{\partial w_1}{\partial x} \\ &- \frac{\partial}{\partial x} \left(-K_0 \frac{\partial T_1}{\partial x} + K_0^* \frac{\partial \nu_1}{\partial x} \right) - \frac{\partial}{\partial y} \left(-K_0 \frac{\partial T_1}{\partial y} + K_0^* \frac{\partial \nu_1}{\partial y} \right) \\ &- \frac{\partial}{\partial z} \left(-K_0 \frac{\partial T_1}{\partial z} + K_0^* \frac{\partial \nu_1}{\partial z} - e_0 \frac{\mathrm{d}T_0}{\mathrm{d}z} \nu_1 - h_0 \frac{\mathrm{d}T_0}{\mathrm{d}z} T_1 + e_0^* \frac{\mathrm{d}\nu_0}{\mathrm{d}z} \nu_1 + h_0^* \frac{\mathrm{d}\nu_0}{\mathrm{d}z} T_1 \right) \\ &- l_0 \nu_1 - m_0 T_1. \end{aligned} \tag{A 5}$$

A.2. *Matrices of the differential eigenvalue problem*

The elements of the matrices that appear in (2.12) are presented below. We give only the non-zero elements of the matrices and primes denote differentiation with respect to z:

$$L_{22} = \eta_0, \quad L_{33} = \eta_0, \quad L_{44} = \xi_0 + \tfrac{4}{3}\eta_0, \quad L_{51} = -K_0^*, \quad L_{55} = K_0,$$

$$\begin{aligned}
&M_{14} = \nu_0, \quad M_{21} = c_0 u_0', \quad M_{22} = \eta_0', \quad M_{24} = \mathrm{i}k_x\left(\xi_0 + \tfrac{1}{3}\eta_0\right), \quad M_{25} = d_0 u_0',\\
&M_{33} = \eta_0', \quad M_{34} = \mathrm{i}k_y\left(\xi_0 + \tfrac{1}{3}\eta_0\right), \quad M_{41} = -a_0, \quad M_{42} = \mathrm{i}k_x\left(\xi_0 + \tfrac{1}{3}\eta_0\right),\\
&M_{43} = \mathrm{i}k_y\left(\xi_0 + \tfrac{1}{3}\eta_0\right), \quad M_{44} = \xi_0' + \tfrac{4}{3}\eta_0', \quad M_{45} = -b_0,\\
&M_{51} = -K_0^{*'} + e_0 T_0' - e_0^* \nu_0', \quad M_{52} = 2\eta_0 u_0', \quad M_{54} = -p_0, \quad M_{55} = K_0' + h_0 T_0' - h_0^* \nu_0',
\end{aligned}$$

$$\begin{aligned}
&N_{11} = \mathrm{i}k_x u_0, \quad N_{12} = \mathrm{i}k_x \nu_0, \quad N_{13} = \mathrm{i}k_y \nu_0, \quad N_{14} = \nu_0',\\
&N_{21} = \tan\theta - \mathrm{i}k_x a_0 + (c_0 u_0)', \quad N_{22} = -\mathrm{i}k_x \nu_0 u_0 - k_x^2\left(\xi_0 + \tfrac{4}{3}\eta_0\right) - k_y^2\eta_0,\\
&N_{23} = -k_x k_y\left(\xi_0 + \tfrac{1}{3}\eta_0\right), \quad N_{24} = -\nu_0 u_0' + \mathrm{i}k_x \eta_0', \quad N_{25} = -\mathrm{i}k_x b_0 + \left(d_0 u_0'\right)',\\
&N_{31} = -\mathrm{i}k_y a_0, \quad N_{32} = -k_x k_y\left(\xi_0 + \tfrac{1}{3}\eta_0\right), \quad N_{33} = -\mathrm{i}k_x \nu_0 u_0 - k_x^2\eta_0 - k_y^2(\xi_0 + \tfrac{4}{3}\eta_0),\\
&N_{34} = \mathrm{i}k_y \eta_0', \quad N_{35} = \mathrm{i}k_y b_0, \quad N_{41} = -1 + \mathrm{i}k_x c_0 u_0' - a_0', \quad N_{42} = \mathrm{i}k_x(\xi_0' - \tfrac{2}{3}\eta_0'),\\
&N_{43} = \mathrm{i}k_y(\xi_0' - \tfrac{2}{3}\eta_0'), \quad N_{44} = -\mathrm{i}k_x \nu_0 u_0 - (k_x^2 + k_y^2)\eta_0, \quad N_{45} = \mathrm{i}k_x d_0 u_0' - b_0',\\
&N_{51} = c_0 u_0'^2 + (k_x^2 + k_y^2)K_0^* + (e_0 T_0')' - (e_0^* \nu_0')' - l_0,\\
&N_{52} = -\mathrm{i}k_x p_0, \quad N_{53} = -\mathrm{i}k_y p_0, \quad N_{54} = -\tfrac{3}{2}\nu_0 T_0' + 2\mathrm{i}k_x \eta_0 u_0',\\
&N_{55} = -\tfrac{3}{2}\mathrm{i}k_x \nu_0 u_0 + d_0 u_0'^2 - (k_x^2 + k_y^2)K_0 + (h_0 T_0')' - (h_0^* \nu_0')' - m_0,
\end{aligned}$$

$$\Sigma_{11} = -1, \quad \Sigma_{22} = \nu_0, \quad \Sigma_{33} = \nu_0, \quad \Sigma_{44} = \nu_0, \quad \Sigma_{55} = \tfrac{3}{2}\nu_0.$$

A.3. *Reduction to a system of first-order equations*

To determine the order of the system (2.12), we seek to reduce it to a system of first-order ordinary differential equations. The linearized mass conservation equation contains only first-order derivatives, and when the normal mode expansion is made it gives a first-order differential equation for $\hat{w}$ which we write as

$$\frac{\mathrm{d}\hat{w}}{\mathrm{d}z} = -\frac{(N_{11} - \sigma\Sigma_{11})}{M_{14}}\hat{v} - \frac{N_{12}}{M_{14}}\hat{u} - \frac{N_{13}}{M_{14}}\hat{v} - \frac{N_{14}}{M_{14}}\hat{w}, \tag{A 6}$$

and differentiation of this equation with respect to z allows us to replace the second-order derivatives of $\hat{w}$ with lower-order derivatives.

In addition, the linearized energy equation contains $\hat{v}''$ and $\hat{T}''$ only in the combination $-K_0\hat{T}'' + K_0^*\hat{v}''$, where primes denote differentiation with respect to z. We therefore introduce a new variable

$$\hat{\beta} = -K_0\hat{v}' + K_0^*\hat{T}', \tag{A 7}$$

which allows us to replace the second-order derivatives in the energy equation with lower-order derivatives.

We are left with a first-order system of the form

$$\boldsymbol{C}\frac{\mathrm{d}\boldsymbol{\phi}}{\mathrm{d}z} = \boldsymbol{D}\boldsymbol{\phi}, \quad \text{where} \quad \boldsymbol{\phi} = (\hat{v}, \hat{u}, \hat{v}, \hat{w}, \hat{T}, \hat{u}', \hat{v}', \hat{\beta})^{\mathrm{T}}, \tag{A 8}$$

and $\boldsymbol{C}$ and $\boldsymbol{D}$ are 8×8 matrices. We conclude that the system of ordinary differential equations (2.12) is an eighth-order system.

The non-zero elements of the matrices are

$$C_{14}=M_{14},\quad C_{21}=M_{21},\quad C_{25}=M_{25},\quad C_{26}=L_{22},$$
$$C_{37}=L_{33},\quad C_{41}=M_{41}-\frac{L_{44}(N_{11}-\sigma\Sigma_{11})}{M_{14}},\quad C_{45}=M_{45},$$
$$C_{51}=M_{51}-L_{51},\quad C_{55}=M_{55}-L_{55},\quad C_{81}=-L_{51},\quad C_{85}=-L_{55},$$

$$D_{11}=\sigma\Sigma_{11}-N_{11},\quad D_{12}=-N_{12},\quad D_{13}=-N_{13},\quad D_{14}=-N_{14},$$
$$D_{21}=\frac{M_{24}(N_{11}-\sigma\Sigma_{11})}{M_{14}}-N_{21},\quad D_{22}=\frac{M_{24}N_{12}}{M_{14}}-(N_{22}-\sigma\Sigma_{22}),$$
$$D_{23}=\frac{M_{24}N_{13}}{M_{14}}-N_{23},\quad D_{24}=\frac{M_{24}N_{14}}{M_{14}}-N_{24},\quad D_{25}=-N_{25},\quad D_{27}=-M_{22},$$
$$D_{31}=\frac{M_{34}(N_{11}-\sigma\Sigma_{11})}{M_{14}}-N_{31},\quad D_{32}=\frac{M_{34}N_{12}}{M_{14}}-N_{32},$$
$$D_{33}=\frac{M_{34}N_{13}}{M_{14}}-(N_{33}-\sigma\Sigma_{33}),\quad D_{34}=\frac{M_{34}N_{14}}{M_{14}}-N_{34},\quad D_{35}=-N_{35},\quad D_{37}=-M_{33},$$
$$D_{41}=\left(\frac{M_{44}}{M_{14}}-\frac{L_{44}M'_{14}}{M_{14}^2}-\frac{L_{44}N_{14}}{M_{14}^2}\right)(N_{11}-\sigma\Sigma_{11})-N_{41}+\frac{L_{44}}{M_{14}}\left(N'_{11}-\sigma\Sigma'_{11}\right),$$
$$D_{42}=\frac{M_{44}N_{12}}{M_{14}}-N_{42}-\frac{L_{44}}{M_{14}^2}\left[N_{12}M'_{14}-N'_{12}M_{14}+N_{12}N_{14}\right],$$
$$D_{43}=\frac{M_{44}N_{13}}{M_{14}}-N_{43}-\frac{L_{44}}{M_{14}^2}\left[N_{13}M'_{14}-N'_{13}M_{14}+N_{13}N_{14}\right],$$
$$D_{44}=\frac{M_{44}N_{14}}{M_{14}}-(N_{44}-\sigma\Sigma_{44})-\frac{L_{44}}{M_{14}^2}\left[N_{14}M'_{14}-N'_{14}M_{14}\right],$$
$$D_{45}=-N_{45},\quad D_{46}=\frac{L_{44}N_{12}}{M_{14}}-M_{42},\quad D_{47}=\frac{L_{44}N_{13}}{M_{14}}-M_{43},$$
$$D_{51}=\frac{M_{54}(N_{11}-\sigma\Sigma_{11})}{M_{14}}-N_{51},\quad D_{52}=\frac{M_{54}N_{12}}{M_{14}}-N_{52},\quad D_{53}=\frac{M_{54}N_{13}}{M_{14}}-N_{53},$$
$$D_{54}=\frac{M_{54}N_{14}}{M_{14}}-N_{54},\quad D_{55}=\sigma\Sigma_{55}-N_{55},\quad D_{56}=-M_{52},$$
$$D_{66}=D_{77}=D_{88}=1.$$

The system of differential equations is singular when $\det(\boldsymbol{C})=0$. The determinant can be expanded easily as

$$\det(\boldsymbol{C})=C_{14}C_{26}C_{37}C_{58}\left(C_{41}C_{85}-C_{45}C_{81}\right),$$

which we can write in terms of the flow quantities as

$$\det(\boldsymbol{C})=-\eta_0^2\left[K_0(\xi_0+\tfrac{4}{3}\eta_0)(\sigma+\mathrm{i}k_x u_0)+a_0\nu_0K_0+b_0\nu_0K_0^*\right]. \tag{A 9}$$

A.4. *Linearized base boundary conditions*

Because the planar surface of the chute is an impenetrable boundary to the flowing grains, we must have $w\equiv 0$ at $z=0$. On linearization we trivially obtain

$$w_1(0,x,y,t)=0, \tag{A 10}$$

and in addition,

$$\left.\frac{\partial w_1}{\partial x}\right|_{z=0} = \left.\frac{\partial w_1}{\partial y}\right|_{z=0} \equiv 0. \tag{A 11}$$

The transfer of momentum and energy between the flowing grains and the stationary base boundary is described by the boundary conditions of Richman (1988)

$$\boldsymbol{M} = \boldsymbol{P}\cdot\boldsymbol{n}, \qquad \boldsymbol{q}\cdot\boldsymbol{n} = -\boldsymbol{M}\cdot\boldsymbol{u} - \mathscr{D}. \tag{A 12}$$

For a fully three-dimensional flow field, the components of the boundary traction force $\boldsymbol{M}$ can be written as

$$M_x = \nu\chi T^{1/2} S_x, \quad M_y = \nu\chi T^{1/2} S_y, \quad M_z = \nu\chi T + \nu\chi T^{1/2} S_z, \tag{A 13}$$

where we define

$$\left.\begin{aligned} S_x &= \sqrt{\frac{2}{\pi}}\left(-\kappa u + \bar{d}\left(\kappa - \frac{1}{2}Ar^2\right)\frac{\partial u}{\partial z}\right), \\ S_y &= \sqrt{\frac{2}{\pi}}\left(-\kappa v + \bar{d}\left(\kappa - \frac{1}{2}Ar^2\right)\frac{\partial v}{\partial z}\right), \\ S_z &= \sqrt{\frac{2}{\pi}}\bar{d}\left(B\frac{\partial w}{\partial z} - \frac{1}{2}Ar^2\frac{\partial u}{\partial x}\right), \end{aligned}\right\} \tag{A 14}$$

with the quantities $A(\nu)$ and $\kappa(r)$ given by

$$A(\nu) = 1 + \frac{\pi}{12\sqrt{2}}\left(1 + \frac{5}{8\nu g_0(\nu)}\right), \quad \kappa(r) = \frac{2}{3}\left(\frac{2}{1+\sqrt{1-r^2}} - \sqrt{1-r^2}\right), \tag{A 15}$$

and where we define

$$B = A(r^2 - 2) + \kappa + 2\sqrt{1-r^2}. \tag{A 16}$$

The boundary dissipation is given as

$$\mathscr{D} = \Delta\nu\chi T^{3/2}, \tag{A 17}$$

where Δ is a function of the boundary geometry, through the roughness parameter r, and the coefficient of restitution in particle–wall collisions, e_w, and is given by

$$\Delta = \sqrt{\frac{2}{\pi}}\frac{2(1-e_w)}{1+\sqrt{1-r^2}}. \tag{A 18}$$

These quantities include the exclusion factor χ, which accounts for the shielding of collisions between particles and the base by other particles in the flow. When considering the steady chute flow in Part 1, we determine χ from the normal stress balance at the base boundary.

The components of the boundary traction force can be linearized by making the expansions

$$S_x = S_{x,0} + S_{x,1}, \qquad S_y = 0 + S_{y,1}, \qquad S_z = 0 + S_{z,1}, \tag{A 19}$$

with

$$\left.\begin{aligned} S_{x,0} &= \sqrt{\frac{2}{\pi}}\left(-\kappa u_0 + \left(\kappa - \frac{1}{2}A_0 r^2\right)\frac{\mathrm{d}u_0}{\mathrm{d}z}\right), & S_{x,1} &= S_x^v v_1 + S_x^u u_1 + S_x^{u_z}\frac{\partial u_1}{\partial z}, \\ S_{y,1} &= S_y^v v_1 + S_y^{v_z}\frac{\partial v_1}{\partial z}, & S_{z,1} &= S_z^u\frac{\partial u_1}{\partial x} + S_z^{w_z}\frac{\partial w_1}{\partial z}, \end{aligned}\right\} \tag{A 20}$$

where

$$\left.\begin{aligned} S_x^v &= -\frac{1}{2}\sqrt{\frac{2}{\pi}}\dot{A}_0 r^2 \frac{\mathrm{d}u_0}{\mathrm{d}z}, & S_x^u &= -\sqrt{\frac{2}{\pi}}\kappa, \\ S_x^{u_z} &= \sqrt{\frac{2}{\pi}}\left(\kappa - \frac{1}{2}A_0 r^2\right), & S_y^v &= -\sqrt{\frac{2}{\pi}}\kappa, \\ S_y^{v_z} &= \sqrt{\frac{2}{\pi}}\left(\kappa - \frac{1}{2}A_0 r^2\right), & S_z^u &= -\frac{1}{2}\sqrt{\frac{2}{\pi}}A_0 r^2, \\ S_z^{w_z} &= \sqrt{\frac{2}{\pi}}B_0, \end{aligned}\right\} \tag{A 21}$$

and $\dot{A}_0 = \mathrm{d}A_0/\mathrm{d}\nu$.

The balance between the normal stress in the flow at the base and the normal component of the boundary traction force,

$$P_{zz} = M_z(\chi), \tag{A 22}$$

can be solved to give an expression for the exclusion factor χ. By determining χ in this way we ensure that the normal stress balance at the boundary is satisfied. At leading order in the perturbation quantities, we find

$$\chi_0 = \frac{p_0}{\nu T_0} = \frac{g_1(\nu_0)}{\nu_0}, \tag{A 23}$$

as we found when considering steady chute flows in Part 1. At first order in the perturbations, we find an expression for χ_1 which we write as

$$\chi_1 = \chi^{\nu}\nu_1 + \chi^{u}\frac{\partial u_1}{\partial x} + \chi^{v}\frac{\partial v_1}{\partial y} + \chi^{\mathrm{T}}T_1 + \chi^{w_z}\frac{\partial w_1}{\partial z}, \tag{A 24}$$

where

$$\left.\begin{aligned} \chi^{\nu} &= \frac{a_0\nu_0 - p_0}{\nu_0^2 T_0}, & \chi^{u} &= -\frac{(\xi_0 - \frac{2}{3}\eta_0)T_0^{1/2} + p_0 S_z^u}{\nu_0 T_0^{3/2}}, \\ \chi^{v} &= -\frac{(\xi_0 - \frac{2}{3}\eta_0)}{\nu_0 T_0}, & \chi^{T} &= \frac{b_0 T_0 - p_0}{\nu_0 T_0^2}, \\ \chi^{w_z} &= -\frac{(\xi_0 + \frac{4}{3}\eta_0)T_0^{1/2} + p_0 S_z^{w_z}}{\nu_0 T_0^{3/2}}. \end{aligned}\right\} \tag{A 25}$$

In these expressions all quantities are to be evaluated at $z = 0$.

Substitution of χ into the shear stress balances and the energy flux condition at the base gives three further boundary conditions to add to the mass flux condition. We make the normal mode approximation, so $\partial/\partial x = \mathrm{i}k_x$ and $\partial/\partial y = \mathrm{i}k_y$, and then the base boundary conditions are written in matrix form as

$$\boldsymbol{Q}\frac{\mathrm{d}\boldsymbol{X}}{\mathrm{d}z} + \boldsymbol{R}\boldsymbol{X} = 0, \tag{A 26}$$

which are applied at $z=0$. The 4×5 matrices $\boldsymbol{Q}$ and $\boldsymbol{R}$ are functions of the steady base flow and their non-zero components are given below:

$$Q_{22}=\eta_0+\nu_0\chi_0 T_0^{1/2}S_x^{u_z}, \qquad Q_{24}=\nu_0 T_0^{1/2}S_{x,0}\chi^{w_z},$$
$$Q_{33}=\eta_0+\nu_0\chi_0 T_0^{1/2}S_y^{v_z},$$
$$Q_{41}=-K_0^*, \qquad Q_{42}=\eta_0 u_0,$$
$$Q_{44}=-\Delta\nu_0 T_0^{3/2}\chi^{w_z}, \qquad Q_{45}=K_0,$$

$$R_{14}=1,$$
$$R_{21}=c_0u_0'+\chi_0 T_0^{1/2}S_{x,0}+\nu_0 T_0^{1/2}S_{x,0}\chi^{\nu}+\nu_0\chi_0 T_0^{1/2}S_x^{\nu},$$
$$R_{22}=\mathrm{i}k_x\nu_0 T_0^{1/2}S_{x,0}\chi^{u}+\nu_0\chi_0 T_0^{1/2}S_x^{u}, \qquad R_{23}=\mathrm{i}k_y\nu_0 T_0^{1/2}S_{x,0}\chi^{\nu},$$
$$R_{25}=d_0u_0'+\nu_0 T_0^{1/2}S_{x,0}\chi^{T}+\tfrac{1}{2}\nu_0\chi_0 T_0^{-1/2}S_{x,0}, \qquad R_{33}=\nu_0\chi_0 T_0^{1/2}S_y^{\nu},$$
$$R_{41}=e_0T_0'-e_0^*\nu_0'+c_0u_0u_0'-\Delta\chi_0 T_0^{3/2}-\Delta\nu_0 T_0^{3/2}\chi^{\nu},$$
$$R_{42}=\eta_0u_0'-\mathrm{i}k_x\Delta\nu_0 T_0^{3/2}\chi^{u}, \qquad R_{43}=-\mathrm{i}k_y\Delta\nu_0 T_0^{3/2}\chi^{\nu},$$
$$R_{45}=h_0T_0'-h_0^*\nu_0'+d_0u_0u_0'-\Delta\nu_0 T_0^{3/2}\chi^{T}-\tfrac{3}{2}\Delta\nu_0\chi_0 T_0^{1/2}.$$

A.5. *Asymptotic free surface boundary conditions*

As the linearized governing equations are posed on a semi-infinite domain, the behaviour at the free surface is given by asymptotic conditions. To determine the asymptotic conditions appropriate for the perturbation variables, we follow the approach of Forterre & Pouliquen (2002), using the behaviour of the steady flow quantities as $z\to\infty$ to simplify the governing equations.

We recall from Part 1 that the volume fraction of the steady flow decays exponentially as $z\to\infty$ so that, from the linearized equation for the conservation of mass, the volume fraction perturbation must also vanish. Forterre & Pouliquen (2002) assume $\nu_1\ll\nu_0\ll 1$ and $\nu_1\sim \mathrm{e}^{-z/T_\infty}$ as $z\to\infty$, which can be shown by making an asymptotic series expansion of the linearized governing equations (Woodhouse 2008). In addition, we find

$$\left.\begin{array}{llll} u_0'\sim\nu_0, & T_0'\sim\nu_0, & p_0\sim\nu_0, & \xi_0\sim\nu_0^2,\\ \eta_0\sim\eta_\infty, & K_0\sim K_\infty, & K_0^*\sim K_\infty^*, & \gamma_0\sim\nu_0^2, \end{array}\right\} \tag{A 27}$$

as $z\to\infty$, where η_∞, K_∞ and K_∞^* are constants. We make use of this behaviour to eliminate vanishingly small terms from the linearized equations.

As $z\to\infty$, the linearized momentum equations in the downslope, cross-slope and normal directions become

$$\frac{\partial}{\partial x}\left(\frac{4}{3}\frac{\partial u_1}{\partial x}-\frac{2}{3}\frac{\partial v_1}{\partial y}-\frac{2}{3}\frac{\partial w_1}{\partial z}\right)+\frac{\partial}{\partial y}\left(\frac{\partial u_1}{\partial y}+\frac{\partial v_1}{\partial x}\right)+\frac{\partial}{\partial z}\left(\frac{\partial u_1}{\partial z}+\frac{\partial w_1}{\partial x}\right)=0, \tag{A 28}$$

$$\frac{\partial}{\partial x}\left(\frac{\partial v_1}{\partial x}+\frac{\partial u_1}{\partial y}\right)+\frac{\partial}{\partial y}\left(-\frac{2}{3}\frac{\partial u_1}{\partial x}+\frac{4}{3}\frac{\partial v_1}{\partial y}-\frac{2}{3}\frac{\partial w_1}{\partial z}\right)+\frac{\partial}{\partial z}\left(\frac{\partial v_1}{\partial z}+\frac{\partial w_1}{\partial y}\right)=0, \tag{A 29}$$

$$\frac{\partial}{\partial x}\left(\frac{\partial w_1}{\partial x}+\frac{\partial u_1}{\partial z}\right)+\frac{\partial}{\partial y}\left(\frac{\partial w_1}{\partial y}+\frac{\partial v_1}{\partial z}\right)+\frac{\partial}{\partial z}\left(-\frac{2}{3}\frac{\partial u_1}{\partial x}-\frac{2}{3}\frac{\partial v_1}{\partial y}+\frac{4}{3}\frac{\partial w_1}{\partial z}\right)=0. \tag{A 30}$$

The linearized energy equation in the limit $z \to \infty$ becomes

$$\frac{\partial}{\partial x}\left(\frac{\partial T_1}{\partial x}\right) + \frac{\partial}{\partial y}\left(\frac{\partial T_1}{\partial y}\right) + \frac{\partial}{\partial z}\left(\frac{\partial T_1}{\partial z}\right) = 0. \tag{A 31}$$

On making the normal mode expansion, (A 28)–(A 30) becomes a system of coupled second-order ordinary differential equations

$$\frac{\mathrm{d}^2\hat{u}}{\mathrm{d}z^2} + \frac{1}{3}\mathrm{i}k_x\frac{\mathrm{d}\hat{w}}{\mathrm{d}z} - \left(\frac{4}{3}k_x^2 + k_y^2\right)\hat{u} - \frac{1}{3}k_xk_y\hat{v} = 0, \tag{A 32}$$

$$\frac{\mathrm{d}^2\hat{v}}{\mathrm{d}z^2} + \frac{1}{3}\mathrm{i}k_y\frac{\mathrm{d}w}{\mathrm{d}z} - \frac{1}{3}k_xk_y\hat{u} - \left(k_x^2 + \frac{4}{3}k_y^2\right)\hat{v} = 0, \tag{A 33}$$

$$\frac{\mathrm{d}^2\hat{w}}{\mathrm{d}z^2} + \frac{1}{4}\mathrm{i}k_x\frac{\mathrm{d}\hat{u}}{\mathrm{d}z} + \frac{1}{4}\mathrm{i}k_y\frac{\mathrm{d}\hat{v}}{\mathrm{d}z} - \frac{3}{4}\left(k_x^2 + k_y^2\right)\hat{w} = 0. \tag{A 34}$$

The energy equation (A 31) becomes

$$\frac{\mathrm{d}^2\hat{T}}{\mathrm{d}z^2} - \left(k_x^2 + k_y^2\right)\hat{T} = 0. \tag{A 35}$$

Solving the system we find that the velocity components, which decay in the limit $z \to \infty$, are given by

$$\hat{u} = (U_{10} + U_{11}z)\,\mathrm{e}^{-Kz}, \quad \hat{v} = (V_{10} + V_{11}z)\,\mathrm{e}^{-Kz}, \quad \hat{w} = (W_{10} + W_{11}z)\,\mathrm{e}^{-Kz}, \tag{A 36}$$

for $z \gg 1$, where $K = \sqrt{k_x^2 + k_y^2}$ and

$$V_{10} = -\frac{k_x}{k_y}U_{10} - \frac{\mathrm{i}K}{k_y}W_{10} - \frac{7K}{k_xk_y}U_{11}, \qquad V_{11} = \frac{k_y}{k_x}U_{11}, \qquad W_{11} = \frac{\mathrm{i}K}{k_x}U_{11}. \tag{A 37}$$

The energy equation can be solved simply to give

$$\hat{T} = T_{10}\mathrm{e}^{-Kz}. \tag{A 38}$$

The constants U_{10}, U_{11}, W_{10} and T_{10} remain undetermined. We note that the perturbed velocity and temperature fields decay exponentially to zero, with the decay rate determined by the wavenumbers of the perturbation, and for sufficiently small wavenumbers the fields decay to zero more slowly than the underlying steady flow.

REFERENCES

Alam, M. 2006 Streamwise structures and density patterns in rapid granular Couette flow: a linear stability analysis. *J. Fluid Mech.* **553**, 1–32.

Alam, M., Arakeri, V. H., Nott, P. R., Goddard, J. D. & Herrmann, H. J. 2005 Instability-induced ordering, universal unfolding and the role of gravity in granular Couette flow. *J. Fluid Mech.* **523**, 277–306.

Alam, M. & Nott, P. R. 1998 Stability of plane Couette flow of a granular material. *J. Fluid Mech.* **377**, 99–136.

Anderson, E., Bai, Z., Bischof, C., Blackford, S., Demmel, J., Dongarra, J., Du Croz, J., Greenbaum, A., Hammarling, S., McKenney, A. & Sorensen, D. 1999 *LAPACK Users' Guide*, 3rd edn. Society for Industrial and Applied Mathematics.

Boyd, J. P. 2000 *Chebyshev and Fourier Spectral Methods*, 2nd edn. Dover.

Conway, S. L. & Glasser, B. J. 2004 Density waves and coherent structures in granular Couette flows. *Phys. Fluids* **16** (3), 509–529.

Drazin, P. G. & Reid, W. H. 1981 *Hydrodynamic Stability*. Cambridge University Press.

Forterre, Y. & Pouliquen, O. 2001 Longitudinal vortices in granular flows. *Phys. Rev. Lett.* **86** (26), 5886–5889.

Forterre, Y. & Pouliquen, O. 2002 Stability analysis of rapid granular chute flows: formation of longitudinal vortices. *J. Fluid Mech.* **467**, 361–387.

Goldhirsch, I. & Zanetti, G. 1993 Clustering instability in dissipative gases. *Phys. Rev. Lett.* **70** (11), 1619–1622.

Golub, G. H. & Van Loan, C. F. 1989 *Matrix Computations*, 2nd edn. The Johns Hopkins University Press.

Hopkins, M. A. & Louge, M. Y. 1991 Inelastic microstructure in rapid granular flows of smooth disks. *Phys. Fluids* A **3** (1), 47–57.

Jenkins, J. T. 2007 Dense inclined flows of inelastic spheres. *Granul. Matter* **10**, 47–52.

Kumaran, V. 2008 Dense granular flow down an inclined plane: from kinetic theory to granular dynamics. *J. Fluid Mech.* **599**, 121–168.

Liss, E. D., Conway, S. L. & Glasser, B. J. 2002 Density waves in gravity-driven granular flow through a channel. *Phys. Fluids* **14** (9), 3309–3326.

Lun, C. K. K., Savage, S. B., Jeffrey, D. J. & Chepurniy, N. 1984 Kinetic theories for granular flow: inelastic particles in Couette flow and slightly inelastic particles in a general flowfield. *J. Fluid Mech.* **140**, 223–256.

Malik, M. R. 1990 Numerical methods for hypersonic boundary layer stability. *J. Comput. Phys.* **86** (2), 376–413.

McNamara, S. & Young, W. R. 1994 Inelastic collapse in two dimensions. *Phys. Rev.* E **50** (1), 28–31.

Mitarai, N. & Nakanishi, H. 2001 Instability of dilute granular flows on rough slope. *J. Phys. Soc. Japan* **70** (10), 2809–2812.

Mitarai, N. & Nakanishi, H. 2004 Linear stability analysis of rapid granular flow down a slope and density wave formation. *J. Fluid Mech.* **507**, 309–334.

Moler, C. B. & Stewart, G. W. 1973 An algorithm for generalised matrix eigenvalue problems. *SIAM J. Numer. Anal.* **10** (2), 241–256.

Richman, M. W. 1988 Boundary conditions based upon a modified Maxwellian velocity distribution for flows of identical, smooth, nearly elastic spheres. *Acta Mech.* **75**, 227–240.

Savage, S. B. 1992 Instability of unbounded uniform granular shear flow. *J. Fluid Mech.* **241**, 109–123.

Schmid, P. J. & Kytömaa, H. K. 1994 Transient and asymptotic stability of granular shear flow. *J. Fluid Mech.* **264**, 255–275.

Sela, N. & Goldhirsch, I. 1998 Hydrodynamic equations for rapid flows of smooth inelastic spheres, to Burnett order. *J. Fluid Mech.* **361**, 41–74.

Tan, M.-L. & Goldhirsch, I. 1997 Intercluster interactions in rapid granular shear flows. *Phys. Fluids* **9** (4), 856–869.

Wang, C.-H., Jackson, R. & Sundaresan, S. 1996 Stability of bounded rapid shear flows of a granular material. *J. Fluid Mech.* **308**, 31–62.

Wang, C.-H., Jackson, R. & Sundaresan, S. 1997 Instabilities of fully developed rapid flow of a granular material in a channel. *J. Fluid Mech.* **342**, 179–197.

Woodhouse, M. J. 2008 Rapid granular shear flows. PhD thesis, School of Mathematics, University of Bristol, Bristol.

Woodhouse, M. J., Hogg, A. J. & Sellar, A. A. 2010 Rapid granular flows down inclined planar chutes. Part 1. Steady flows, multiple solutions and existence domains. *J. Fluid Mech.* (in press).